

ACOUSTIC-STRUCTURAL INTERACTION:
UNDERSTANDING AND APPLICATIONS IN SENSOR
DEVELOPMENT AND METAMATERIALS

A Dissertation
Submitted to
the Temple University Graduate Board

In Partial Fulfillment
of the Requirements for the Degree
DOCTOR OF PHILOSOPHY

by
QIAN DONG
August 2021

Examining Committee Members:

Dr. Haijun Liu, Advisory Chair, Department of Mechanical Engineering

Dr. Ling Liu, Department of Mechanical Engineering

Dr. Albert Kim, Department of Electrical and Computer Engineering

External Member

Dr. Yimin Zhang, Department of ECE, Temple University

ABSTRACT

Acoustic-structural interaction is the key to understand a wide range of engineering problems such as membrane-based dynamic pressure sensors, hearing devices for sound source localization, and acoustic absorbers for noise reduction. Despite tremendous developments in the last decades, there is still a fundamental size limitation in these areas. In the case of dynamic pressure sensors, sensitivity usually suffers for miniature sensors; the available acoustic directional cues proportionally decrease with size, which adversely affects the localization performance; thick panels are required to achieve superior sound attenuation, particularly for low frequency sound. It is the motivation of this dissertation research to address the abovementioned size limitation that involves acoustic-structural interaction.

The overall goal of this dissertation work is to achieve an enhanced understanding of the acoustic-structural interaction between diaphragms and air cavity and to apply this understanding to develop high-performance miniature acoustic sensors and noise reduction metamaterials. First, a finite element method (FEM) model and large-scale device are developed to understand how the interaction between the diaphragm and its backing air cavity affects the equivalent mass, stiffness, and damping of air-backed diaphragms. The numerical and experimental study shows that the complex interaction cannot be captured by the commonly used lump model. Then, air-backed graphene diaphragms are used to develop fiber optic sensors with sub-millimeters footprint and high sensitivity. Two different configurations are designed to enhance the sensor

sensitivity limited by the backing air cavity. One is to increase the mechanical sensitivity by using a larger backing volume, the other is to increase the optical sensitivity by using silver-graphene composite diaphragm. Next, acoustic metamaterials with air-coupled diaphragms as unit cells are developed to achieve perfect acoustic absorption with thickness much smaller than the sound wavelength, which cannot be realized using natural materials. Finally, an expanded configuration of two diaphragms coupled by an air-filled tunnel is experimentally developed to mimic the hearing system of small vertebrates. The goal is to amplify the small directional cues available to the small animals so that a high angular resolution can be achieved.

This dissertation provides a quantitative and mechanistic explanation for the interaction between the diaphragms and the sealed air cavity. It offers several frameworks for the development of miniature pressures, directional sensors, and thin sound absorbers.

DEDICATION

To my parents

To the Cat

To the past

ACKNOWLEDGMENTS

First and foremost, I would like to express my sincere gratitude to my advisor, Dr. Haijun Liu. It is his encouragement, insights, and support that have guided me through the five years. Whenever I was frustrated with the problems encountered in experiments or simulations, he is always there to help me with his thorough knowledge and generous patience. The experience working with him benefited me and kept guiding me in my future work.

I am most thankful to other professors in my dissertation committee, Dr. Ling Liu, Dr. Albert Kim, and Dr. Yimin Zhang.

I also want to thank all the colleagues and friends around me, XiaoLei Song, Ray Subhrodeep, Ye Yao, Tiara Zhang, Teng Qu, Yujia Guo, Fangchu Nie, Fangzhou Zheng, Nani He, and fellows from New Haven. Their friendship encourages me to start and finish this journey and makes my life at State enjoyable and memorable. I also want to thank Dr. George Collins, who inspired and encouraged me to pursue this fantastic path.

My deepest gratitude goes to my parents for their unconditional love and support through the years, and Nani for being in my life.

TABLE OF CONTENTS

ABSTRACT.....	ii
DEDICATION.....	iv
ACKNOWLEDGMENTS	v
LIST OF TABLES.....	x
LIST OF FIGURES	xi
CHAPTER 1: INTRODUCTION AND BACKGROUND.....	1
1.1 Problem of Interest and Motivation	1
1.1.1 Dynamic Pressure Sensors.....	1
1.1.2 Directional Acoustic Sensors.....	3
1.1.3 Membrane-Based Metamaterials for Sound Absorption	5
1.2 Objectives and Scope of the Proposed Work.....	6
CHAPTER 2: UNDERSTANDING ACOUSTIC-STRUCTURAL INTERACTION .	9
2.1 Introduction.....	9
2.2 Experiment Design.....	14
2.3 Experimental Results	17
2.3.1 Finite Element Simulation	17
2.3.2 Experimental Verification.....	22

2.4 Summary	27
CHAPTER 3: MINIATURE DYNAMIC PRESSURE SENSORS WITH A GRAPHENE DIAPHRAGM	30
3.1 Introduction.....	30
3.2 Fiber Optic Sensors with Graphene-Silver Composite Diaphragms	37
3.2.1 Fabrication	37
3.2.2 Experimental Characterization.....	40
3.3 Finite Element Simulation	46
3.4 Fiber Optic Sensors with Graphene Diaphragm and Enlarged Backing Air Cavity.....	49
3.4.1 Fabrication Process	50
3.5 Summary.....	52
CHAPTER 4: DIRECTIONAL ACOUSTIC SENSORS INSPIRED BY INTERNALLY COUPLED EARS.....	55
4.1 Introduction.....	55
4.1.1 Directional Hearing in Animals	57
4.1.2 Internally Coupled Ears (ICE)	58
4.1.3 Lumped Model for Air-born Coupling ear	59
4.1.4 Transmission Gain (TG) Calculation.....	61

4.2 Design of Bio-inspired Pressure Different Receiver	62
4.3 Sensor Fabrication and Integration	66
4.4 Sensor Characterization	67
4.5 Summary	69
 CHAPTER 5: ACOUSTIC METAMATERIALS WITH AIR-COUPLED DIAPHRAGMS	 70
5.1 Introduction.....	70
5.2 Theoretical Framework Using Impedance Matching	72
5.3 AMM Design Using Numerical Simulation	77
5.4 Experimental Results	81
5.4.1 Tuning by Varying Cavity Length.....	81
5.4.2 Tuning by Using Micro-Perforated Plates (MPP)	83
5.4.3 Tuning by Using Lighter Porous Materials (Silica Aerogel).....	84
5.5 Summary	85
 CHAPTER 6: SUMMARY.....	 87
Thrust 1: Understanding of acoustic-structural interaction	87
Thrust 2: Development of fiber optic sensor with air-backed graphene diaphragm	87

Thrust 3: Development of acoustic sensors mimicking internally coupled ears	88
Thrust 4: Development of acoustic metamaterials with air-coupled diaphragms	88
BIBLIOGRAPHY	90

LIST OF TABLES

Table 2.1: Properties of the polyimide diaphragm/Paagm	20
Table 3.1: Comparison of properties and performance of different diaphragm materials for acoustic sensors	36
Table 3.2: Effects of silver on graphene-based acoustic sensors	44
Table 4.1: Physical parameters for a cavity-coupled auditory system.....	63
Table 5.1: Parameters for the analytical lumped model	76

LIST OF FIGURES

<p>Figure 1.1: Two types of microphones: (a) Omni-directional pressure microphone (b) Directional pressure different receiver (Beranek 1954).....</p>	3
<p>Figure 2.1: Introduction of the studied problem. (a) Schematic of a circular clamped diaphragm backed by a cylindrical air cavity, which has a rigid sidewall and bottom. (b) The mode shapes of the first two axisymmetric modes of the diaphragm (top) and air cavity (bottom).....</p>	11
<p>Figure 2.2: Experiment design to investigate structural-acoustical interaction: (a) Schematic of the setup to vary the backing air cavity length; (b) photo image of the polyimide diaphragm with its edge-glued to a circular steel shim (next to a dime); (c) photo image of the integrated device under test (DUT) mounted on a stage; (d) schematic of the measurement system including a low-coherence fiber-optic interferometer (LCFOI) system in the shaded area.....</p>	15
<p>Figure 2.3: Finite element model (FEM) model and simulation results. (a) FEM model in COMSOL. (b) Mode shape (fundamental) for the three cavity lengths ($l = 0.3$ mm, 3 mm, and 20 mm) obtained using an eigenfrequency study in the COMSOL Pressure Acoustics (PA) module. (c) Mechanical sensitivity as a function of frequency for the three cavity lengths obtained using (PA, solid line) and the Thermoviscous Acoustics (TA, dashed line) module. (d–g) Field distribution of the magnitudes of the velocity in the normal/z-direction (top), the velocity in the tangential/radial direction (middle), and the acoustic pressure (bottom) for four cases: (d): PA, $l = 0.3$ mm; (e) TA, $l = 0.3$ mm; (f) PA, $l = 20$ mm; and (g) TA, $l = 20$ mm. The frequency for all cases in (d–g) was 1.3.</p>	19
<p>Figure 2.4 Experimental results in comparison with the simulations. (a–d): Frequency response function (i.e., mechanical sensitivity as a function of frequency) for different cavity lengths ($l = 20$ mm, 10 mm, 0.8 mm, and 0.3 mm), where the simulation results were obtained using the COMSOL Thermoviscous Acoustics module. The insets show the mode shapes for the fundamental mode. (e–g): mechanical sensitivity (e), natural frequency (f), and damping ratio (g) as a function of cavity length. The curves in the bottom of (e–g) show the slopes.....</p>	24
<p>Figure 2.5 Parametric study by changing the in-plane tension in the diaphragm via thermal expansion and cooling: (a,b) Contour plot of sensitivity as a function of cavity length l and shrinkage temperature ΔT (top (a): experiment, bottom (b): simulation (b)). (c,d): same as (a,b) but for the natural frequency; (e,f): Mechanical sensitivity (e) and</p>	

natural frequency (f) as a function of ΔT for three different cavity lengths 0.5 mm, 2 mm, and 20 mm (scatter points: experiment, lines: simulation). (g) Natural frequencies of the first two modes of the diaphragm in vacuo (denoted as $fd1$ and $fd2$) and the first fundamental frequency of air-backed diaphragm with $l = 2$ mm, denoted as $ffc1$.
26

Figure 3.1 Air-backed diaphragms for acoustic pressure sensors. (a) Schematic of a circular clamped diaphragm backed by a cylindrical air cavity with rigid side and bottom walls; (b) natural frequencies of using different materials to achieve the same sensitivity without considering the effect of the backing cavity ($L = 67 \mu\text{m}$, $R = 40 \mu\text{m}$).33

Figure 3.2 Ultraviolet-molded fiber optic sensors with graphene (or graphene-silver composite) diaphragms. (a) SEM image of the sensor with its schematic shown in the inset; (b) fabrication process of the molded cavity; (c) schematic of transferring graphene film onto the molded cavity.39

Figure 3.3 Experimental characterization of UV-molded graphene-based fiber optic sensors. (a) Experimental setup with a low coherence fiber optic interferometric system; (b) reflectivity of the Fabry-Perot interferometer of the sensor head; (c) frequency response of sensors with two different kinds of diaphragms (dots for experiments, and lines for simulation); (d) time domain signals at 2 kHz from the reference microphone (top), fiber optic sensor with graphene only as the diaphragm (middle), and sensor with graphene and silver composite diaphragm (bottom), all of which are normalized to have an amplitude of one; (e) Fourier transform of the signals in (d).....42

Figure 3.4 Numerical simulation to obtain the frequency response for the fabricated fiber optic sensors using COMSOL. (a): FEM model using COMSOL Multiphysics; (b)&(c): mechanical sensitivity as a function of frequency, comparing two kinds of FEM simulations with the experiment results, for the sensors with graphene-only (b) and graphene-silver composite (c) films; (d)-(e): cross-section views of velocity fields (normal (d) and tangential (e)) for the fiber optic sensor with graphene-only diaphragm at 2 kHz, obtained using pressure acoustics simulation in COMSOL where loss is neglected; (f)-(g): velocity fields (normal (f) and tangential (g)) for the same sensor and same frequency as in (d)-(e) but obtained using thermoacoustics simulation in COMSOL where thermal and viscous losses are considered.47

Figure 3.5 Fiber optic sensors with enlarged backing air cavity: (a) schematic of the sensor (not to scale), (b) SEM picture, (c) mechanical sensitivity spectrum: dashed line for the simulated sensitivity when there is no side gap, solid line for simulated sensitivity of the fabricated device with $LT=10$ mm, and dots for the experiment data,

(d) mechanical sensitivity at 2 kHz, simulated using COMSOL thermoviscous acoustics, as a function of the length of capillary tube LT (denoted in (a)), (e) comparison of reference microphone and the graphene sensor in time domain at sound frequency 2 kHz, and (f) Fourier transform of the signals in (e).....51

Figure 4.1. Existing ICE model. (a) An auditory system consisting of two simple ears coupled acoustically through a closed cavity. (b) The corresponding lumped model. 60

Figure 4.2. Local stimulation for transmission gain measurement. (a) Step 1: measure pressure P_1 and velocity v_1 of ipsilateral eardrum. (b) Step 2: to measure the closed field pressure P_1' at ipsilateral side and normal velocity v_2' of contralateral eardrum.61

Figure 4.3. Low-frequency auditory models. (a) FEM model using COMSOL Multiphysics. (b) The first two mode shapes: the rocking mode (left) and the bending mode (right), (c) IPD at azimuth 90° as a function of frequency based on the Fletcher model, which is shown in the inset. (d) IPD at 1 kHz as a function of azimuth when the volume of the connecting cavity is varied.65

Figure 4.4: Bio-inspired directional acoustic sensor. (a) Schematic of sensor (top) and a low-coherence fiber-optic interferometric system (bottom). (b) Photo of the sensor before (top) and after (bottom) attaching the diaphragm.....67

Figure 4.5. Characterization of the prototype. (a) Surface plot of IPD comparing the simulation (i) and experimental results (ii). (b) IPD at 90° incident as a function of frequency (inset shows the mode shape for the rocking mode). (c) IPD versus azimuth angles at frequency 1.4 kHz. (d) IPD versus azimuth angles at frequency 2.9 kHz. (e) Calculation of the average directional sensitivity (ADS).68

Figure 5.1: Acoustic metamaterial thin panel for broadband acoustic absorption. Schematic of the panel (a) and unit cell (b), whose dimensions are shown in (c) and lumped model in (d).....73

Figure 5.2 Absorption properties of AMM obtained from the analytical lumped model. (a) Absorption spectra for three different values of impedance matching factor β ($\beta = 1$ for the matched impedance case). (b) Maximum absorption as a function of β . (c) Absorption spectra for three different values of mass factor η when $\beta = 1$ (the bigger the value of η , the heavier the effective mass). (d) Absorption bandwidth as a function of η75

Figure 5.3: Tuning the effective damping using a straight cylindrical air cavity. (a) FEM model in COMSOL. (b) Mode shape of the fundamental mode before (top) and after (bottom) hybridization. (c) Impedance matching factor β as a function of cavity length h_c for three different shrinkage temperatures ΔT . (d) β as a function of the static pressure in the cavity for three different h_c values. 78

Figure 5.4: Tuning the effective damping by adding a perforated plate and changing its thickness. Inset shows the schematic in COMSOL. 80

Figure 5.5: Preliminary experimental results. (a) Experimental setup based on an impedance tube (B&K Type 4206). (b) Absorption spectrum for a prototype with 17 mm length cavity..... 82

Figure 5.6: Experimental results for adding an MPP inside the cavity. (a) Photo of an MPP inside the cylindrical cavity; (b) absorption spectra for different diameters for the MPP hole (top); (bottom) three damping factories as a function of frequencies..... 84

Figure 5.7: Preliminary experimental results for aerogel membrane. 85

CHAPTER 1: INTRODUCTION AND BACKGROUND

1.1 Problem of Interest and Motivation

1.1.1 Dynamic Pressure Sensors

Highly integrated and miniature systems are desired in acoustic sensing. Although there are several sensing mechanisms for dynamic pressure sensors, such as piezo-resistive, capacitive, and optical techniques (Eaton and Smith 1997), the main component of the vibrating structure is still typically a thin diaphragm that vibrates in response to pressure excitation, which is converted to an electrical output. For example, in dealing with audio-frequency, generally established from 20 Hz to 20 kHz, a flexible diaphragm can be easily found in condenser microphones, as shown in Figure 1.1. The vibration of the diaphragm involves acoustic-structural interaction (ASI) between a circular diaphragm and its backing air cavity.

ASI has profound effects on the dynamics of the diaphragm. In one previous study (M. Yu and Balachandran 2005), the sensor diaphragm involving acoustically caused dynamic vibration in the audible range has been generally modeled as a circularly clamped plate under certain in-plate tension. Describing the air cavity using scalar wave equation, Gorman et al. (Gorman et al. 2001a) found that a strong ASI occurs when the acoustic and structural subsystems have close natural frequencies and affined mode shapes. However, the damping, due to the viscous loss of the boundary between fluid air and cylinder walls, was considered to be negligible. This assumption is valid when

the dimensions of the backing cavity are much larger than the thickness of viscous boundaries. For the prototypes used by Gorman, the diameter is 76 mm, the cavity length is 81 mm for the sample with short cavity (255 mm for the one with long cavity). In comparison, the thermal/viscous boundary layer thickness is 49 μm at 2 kHz. On the other hand when the air cavity is very thin, Reynolds equations are usually used to study ASI (Skvor 1969; Bao and Yang 2007a), where the viscous loss, referred as the squeeze film damping (Andrews 1993), has to be considered.

Regardless of the equations used to model ASI, it can be lumped as a single-degree-of-freedom system with an equivalent mass, spring, and damper. Compared with the diaphragm in *vacuo* (i.e., neglecting the effects of the backing air cavity), it is important to investigate the change of the abovementioned equivalent parameters. In another study (Liu, Olson, and Yu 2014), an analytical model is developed to predict sensor performances (including the working bandwidth and mechanical sensitivity), which is validated by finite element simulations. On the scaling of natural frequency with decreasing air cavity length, it has a rather complicated three-stage relationship with the cavity length. This study is important for designing miniature acoustic sensors when traditional models are inadequate to predict the sensor performance.

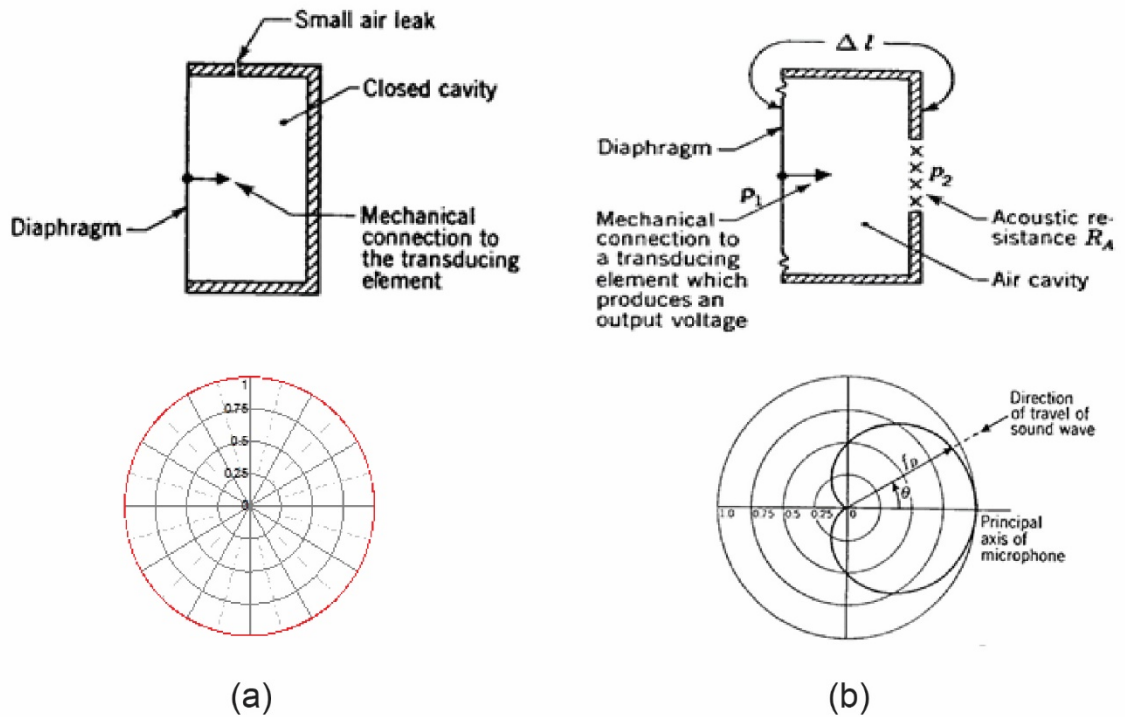


Figure 1.1: Two types of microphones: (a) Omni-directional pressure microphone (b) Directional pressure different receiver (Beranek 1954).

1.1.2 Directional Acoustic Sensors

Directional acoustic sensors are used to determine the direction of sound source, which has two main approaches. One is to form an array of the omni-directional microphones shown in Figure 1.1a, the other is to use an inherently directional microphone, as shown in Figure 1.1b, which has both surfaces of the diaphragm exposed to the external source.

The simplest form of the first approach is a microphone pair, from which the time difference of arrival (TDOA) can be used to determine the sound source direction (Benesty, Chen, and Huang 2008). A similar example is human's auditory system with two symmetrically located sensors (i.e., ears). For an adult with average head width of 20 cm, TDOA is 0.6 ms. In order to determine the sound source direction, the separation of microphones needs to be larger than a critical value, which is affected by various factors such as signal-to-noise ratio (SNR), choice of estimator, and number of samples.

On the other hand, the pressure gradient microphone is an inherently directional system (Figure 1.1b). A cardioid shape directional pattern, which shows the pressure variations as a function of azimuth angles, can be generated. However, as the effective distance ΔL decreases to be much smaller than the wavelength, the directional pattern will reduce to be omni-directional. In other words, the sound source localization performance also will suffer when the size decreases.

To address the fundamental size constraint, one may look into nature for inspiration, particularly small animals such as reptiles (Wever 1987) and birds (Dooling, Lohr, and Dent 2000). In the auditory system of these animals, an interaural channel through their oral cavity connects two eardrums. For each eardrum, both the outer and inner sides are exposed to the sound stimuli: the sound reaches the inner side of one eardrum through the vibration of the other eardrum and propagation through the connecting channel. In other words, these are internally coupled ears (ICE). Deep understanding of ASI is the

key to apply the bioinspired ICE mechanism for developing miniature directional acoustic sensors.

1.1.3 Membrane-Based Metamaterials for Sound Absorption

The term metamaterial was initially defined as man-structured composites, which can manipulate waves beyond the prescribed limits found in nature (G. Ma and Sheng 2016). It was first derived and practiced to manipulate the electromagnetic waves through a periodical structure called photonic crystal (Yablonovitch 1987; Yablonovitch 1989). Similarly, acoustic metamaterials (AM) are also built by the periodically arranged unit cells. Since the first realization of AM (Sheng et al. 2003), AM has evolved from realizing the negative effective mass (Milton and Willis 2007) and negative bulk modulus (J. Li and Chan 2004), to real applications such as the acoustic super-lens (Kaina et al. 2015), acoustic cloaking (Zhang, Xia, and Fang 2011), phase manipulation (Y. Li et al. 2013), and sound absorption (G. Ma et al. 2014).

Due to the lightweight and simple configuration, membrane-based metamaterials (MAM) have dominated the applications operating at a low audible frequency regime, specifically from 0.05 kHz to 2 kHz (G. Ma and Sheng 2016). In this frequency range, the sound wavelength is from few meters to hundreds of millimeters, much larger than the size of membranes, which is no more than a few centimeters generally. Hence, this deep sub-wavelength characteristic of MAM makes it an excellent candidate to address the fundamental size constraint, e.g., in sound absorption. Conventional absorption

foams made by sponges, wools, or fibers dissipate sound energy by the internal frictions due to the interaction between sound's flow and foams' microstructure, which makes sound dissipation much more difficult for low frequency sound. To this end, MAM provides a new approach to address the size limitation in low-frequency sound absorption. However, current reported MAM suffers from the very limited bandwidth of absorption. For example in one of the recent studies (G. Ma et al. 2014), three total absorption bands are achieved at three frequencies, 261 Hz, 310 Hz, and 419 Hz, but the bandwidth is only 1 to 2 Hz.

1.2 Objectives and Scope of the Proposed Work

Although the acoustic-structural interaction is essential in a variety of fields, this dissertation seeks to answer the following critical question in relationship to the size limitation: i) How does the miniaturization affects the performance of pressure sensors constructed with air-backed diaphragms? ii) If sensor performance is constrained by the backing cavity, are there solutions to overcome this limitation to achieve high performance? iii) Can the internal coupling mechanism found in Nature be used to develop miniature directional acoustic sensors with high performance? iv) Can acoustic-structural interaction be explored for developing thin but broadband sound absorbers?

The dissertation research aims to develop a deep understanding of the acoustic-structural interaction between diaphragm and air and use the gained insights to develop

high-performance pressure sensors, directional sensors, and metamaterials. The dissertation work includes the following four research thrusts:

- **Thrust 1: Fundamental understanding of acoustic-structural interaction**

In this Thrust (Chapter 2), a large-scale pressure sensor consisting of a thin clamped circular diaphragm and a backing cavity with tunable length will be constructed as a representative structure to investigate the acoustic-structural interaction. The center deflection of the diaphragm will be detected by a low-coherence fiber-optic interferometer system. Different in-plane tension will be applied to the diaphragm in a parametric study. The goal is to study how the air cavity affects the diaphragm's effective properties, such as density, damping, and stiffness.

- **Thrust 2: Development of fiber optic sensor with air-backed graphene diaphragm**

In this Thrust (Chapter 3), graphene-based acoustic pressure sensors will be developed on the tip of optical fibers with a sub-millimeter footprint. The goal is to address the limitation of sensitivity of sensors with short air cavity, where the sensor's mechanical sensitivity is limited by the air cavity (in other words, the stiffness of the air cavity dominates that of the diaphragm). Two approaches will be adopted: one is focusing on improving the optical reflectivity, the other is to increase the mechanical sensitivity.

- **Thrust 3: Development of acoustic sensors mimicking internally coupled ears**

In this Thrust (Chapter 4), a directional acoustic sensor will be developed to mimic the internally coupled ears. Targeting the application of sound source localization, this inherently directional acoustic sensor will be much smaller than the sound wavelength but can achieve high directional sensitivity. The key is to utilize the internal coupling mechanism found in animals like lizards to amplify the directional cues acoustically.

- **Thrust 4: Development of acoustic metamaterials with air-coupled diaphragms**

In this Thrust (Chapter 5), the understanding gained from Thrust 1 will be used to develop membrane-based acoustic metamaterials (AMM). The focus will be on a single diaphragm with a backing air cavity for perfect absorption. Different ways to realize 100% absorption will be investigated; AMM will be fabricated and characterized in an acoustic impedance tube. Depending on the pertinent parameters, this design provides a variety of options to tune the acoustic properties.

CHAPTER 2 UNDERSTANDING ACOUSTIC-STRUCTURAL INTERACTION

2.1 Introduction

An air-backed diaphragm is the key structure of most dynamic pressure sensors and plays a critical role in determining sensor performance. The previous analytical model investigated the influence of air cavity length on the sensitivity and bandwidth (Liu, Olson, and Yu 2014b). The model found that as the cavity length decreases, the static sensitivity monotonically decreases, and the fundamental natural frequency shows a three-stage trend: increasing in the long-cavity-length range, reaching a plateau value in the medium-cavity-length range, and decreasing in the short-cavity-length range, which cannot be captured by the widely used lumped model. In this Chapter, we conducted the first experimental measurements to validate these findings. Pressure sensors with a circular polyimide diaphragm and a backing air cavity with an adjustable length were designed, fabricated, and characterized, from which the static sensitivities and fundamental natural frequencies were obtained as a function of the cavity length. A further parametric study was conducted by changing the in-plane tension in the diaphragm. A finite element model was developed in COMSOL to investigate the effects of thermoviscous damping and provide validation for the experimental study.

For dynamic pressure sensors, the transduction method could be piezoelectric (Ried et al. 1993; Ko et al. 2003), piezoresistive (Schellin and Hess 1992), optical (Hall et al. 2007; Miao Yu and Balachandran 2003), or capacitive (Pedersen, Olthuis, and Bergveld

1997; Scheeper et al. 2003), but the key component of most sensors is a flexible diaphragm backed by an air cavity. In light of the recent trend of miniaturizing sensors to be more portable, integrated, and inexpensive (Dahlin 2012; Hierold 2004), a fundamental question needs to be investigated in terms of how the miniaturization affects the sensor performance, such as the sensitivity and bandwidth.

To account for the effects of the air cavity, the most commonly used model is a lumped element model, where the diaphragm is described by a mass–spring–damper system and the backing air cavity acts as an effective spring (Beranek 1954). According to this single-degree-of-freedom (SDOF) model, as the length of the backing cavity decreases, the “air spring” becomes stiffer and therefore the effective stiffness of the diaphragm increases, leading to reduced mechanical sensitivity and increased natural frequency. However, this model breaks down when the cavity length is smaller than some critical value, as explained below.

To fully capture the acoustic–structural interaction, various analytical mechanics models have been developed, which are categorized in terms of how the cavity is modeled: i) using the Reynolds equation for thin viscous fluid films (also referred to as squeeze film damping) (Andrews, Harris, and Turner 1993b; Bao and Yang 2007b), or ii) using the sound wave equation where the viscous term is usually neglected (Rajalingham, Bhat, and Xistris 1995; 1998). Following the second approach, but in the context of dynamic pressure sensors, an analytical model was developed to investigate how the static mechanical sensitivity SS_c and fundamental natural frequency f_{c1}

change when the cavity length l continuously decreases (Liu, Olson, and Yu 2014). Note subscripts d , a , and c are used throughout this chapter to denote the diaphragm, the air, and the coupled system of the air-backed diaphragm, respectively. Using a circular clamped diaphragm backed by a cylindrical air cavity as a representative configuration, as shown in Figure 2.1a, the diaphragm was modeled as a thin-plate with in-plane tension and the air cavity was described using a wave equation in terms of the velocity potential. A geometric compatibility condition is assumed at the diaphragm–air interface, i.e., continuous displacement/velocity in the normal direction.

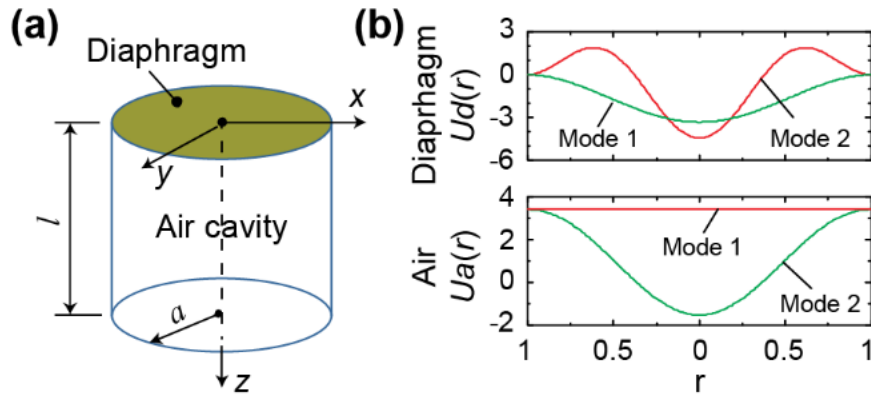


Figure 2.1: Introduction of the studied problem. (a) Schematic of a circular clamped diaphragm backed by a cylindrical air cavity, which has a rigid sidewall and bottom. (b) The mode shapes of the first two axisymmetric modes of the diaphragm (top) and air cavity (bottom)

A key finding from the analytical model was that the air cavity changes the effective stiffness and mass of the diaphragm. A summary is provided here. Assuming that for

small sensors, the diaphragm's radius a is much smaller than the wavelength λ (i.e., $a \ll \lambda$), the transverse (z-direction) displacement excitation at the top of the air cavity can be expressed as $w_a(r, \theta, t) = \sum_{n=0}^{\infty} W_{a,n} U_{a,n} \Theta_0(\theta) e^{j\omega t}$, where the displacement is assumed to be axisymmetric (hence Θ_0 is a constant $\Theta_0(\theta) = 1/\sqrt{2\pi}$), $U_{a,n}(r)$ are the mode shape functions in the radial direction (shown in the bottom of Figure 2.1b for the first two modes along with the first two axisymmetric diaphragm modes at the top), and $W_{a,n}$ are the modal coefficients to be determined. The corresponding reaction pressure from the air to the backside of the diaphragm can be expressed as $p_R(r, \theta, t) = \sum_{n=0}^{\infty} P_{Ra,n} U_{a,n} \Theta_0(\theta) e^{j\omega t}$, where $P_{Ra,n}$ are the coefficients to be determined. When the cavity length is much smaller than the wavelength ($l \ll \lambda$), it can be found that $H_{a,n} = (P_{Ra,n}/p_0)/(W_{a,n}/a)$ is equal to $\gamma a/l$ for the first mode ($n = 0$), where γ is the ration specific heat (1.4 for air), and p_0 is the ambient pressure. The effect of this mode is to increase the effective stiffness of the diaphragm, with the air cavity serving as an equivalent spring. For the second- or higher-order modes ($n \geq 1$), $H_{a,n} \approx -M_{a,n} \Omega_a^2$, where $M_{a,n} = -\left(\frac{\gamma}{\beta_n^2}\right) \left(\frac{a}{l}\right)$, $\Omega_a = \omega a/c_0$ is the normalized frequency, c_0 is the speed of sound in air, and β_n , are the roots of the characteristic equation ($\beta_1 = 3.832, \beta_2 = 7.061$). The effects of these modes are to increase the effective mass of the diaphragm. As l decreases, both the effective stiffness from the first mode and the effective mass from the second and higher-order modes increase, as they scale with $1/l$. Note that if the diaphragm moves like a piston, only the first mode will be excited, and thus, the closed air cavity can be modeled simply as a lumped spring element.

However, when the diaphragm's circumference is clamped, the higher-order modes will be excited. As such, there is an interplay between the stiffness and mass effects as l decreases. The following conclusions were reached for the air-backed diaphragm from the analytical model (Liu, Olson, and Yu 2014), which was validated using finite element method (FEM) simulations in COMSOL: (i) As l decreases, SS_c decreases monotonically. (ii) As l decreases, f_{c1} shows a three-stage trend: it increases in the long-cavity range, reaches a plateau value in the medium-cavity range, and decreases in the short-cavity range. It is important to note that the SDOF lumped model cannot explain these findings.

A related work to experimentally study the effects of an air cavity was carried out by Gorman et al. (Gorman et al. 2001b). A test rig was developed consisting of an aluminum plate (380 μm in thickness and 76 mm in diameter) backed by a cylindrical cavity with a length of 81 mm or 255 mm. The diaphragm was excited by a shaker, its mode shape was observed by Chladni sand method, and two microphones were inserted into the sidewall and base to measure the acoustic pressure. Consistent with the analytical and numerical results, a key conclusion from the study was that strong acoustics–structural interaction exists when the fundamental natural frequencies of the two sub-systems (the diaphragm in vacuo and the closed cavity) are close. However, a comprehensive experimental study is still lacking to systemically investigate the effects of changing air cavity length, particularly in the context of dynamic pressure sensor development.

In this chapter, as a follow-up study to the analytical model (Liu, Olson, and Yu 2014b), the goal is to conduct the first experimental measurements to systemically validate the effects of the air cavity on SS_c and f_{c1} when l continuously decreased, serving as a fundamental guideline for the design and development of dynamic pressure sensors. A parametric study is conducted by varying the in-plane tension, which is a common issue to deal with in sensor fabrication. The experiment results are also validated by comparing them with analytical and numerical simulations.

2.2 Experiment Design

The system used to experimentally investigate the effects of air cavity on sensor performance is illustrated in Figure 2.2. As shown in the cross-section view (Figure 2.2a), the main components included a machined aluminum housing (outside diameter (OD): 76 mm, length: 86 mm), a machined aluminum sliding piston, a circular polyimide diaphragm clamped to a steel shim (inside diameter (ID): 38 mm, OD: 54 mm, thickness: 0.82 mm), and two endcaps (front and back). The housing had an internal cavity with a diameter of 38 mm and a length of 30 mm. The piston had a clearance fit with the housing and was pushed against two springs using a micrometer drive (Newport SM-50 Vernier micrometer, 10 μm increment) attached to the back endcap, providing a turning mechanism to vary the length of the backing air cavity. The front endcap was fabricated using a 3D printer (Ultimaker 3 Extended) using a polylactic acid (PLA) filament. Sound could reach the diaphragm through the large openings on the front endcap. A ceramic ferrule (Thorlabs CFLC128, ID: 128 μm) was

press-inserted into a center hole on the front endcap, which was used to guide an optical fiber for detecting the center displacement of the diaphragm.

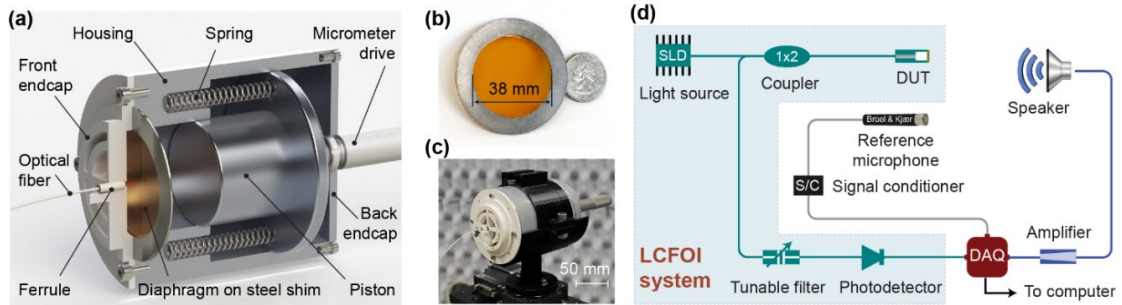


Figure 2.2: Experiment design to investigate structural-acoustical interaction: (a) Schematic of the setup to vary the backing air cavity length; (b) photo image of the polyimide diaphragm with its edge-glued to a circular steel shim (next to a dime); (c) photo image of the integrated device under test (DUT) mounted on a stage; (d) schematic of the measurement system including a low-coherence fiber-optic interferometer (LCFOI) system in the shaded area.

Thermal stress was generated to adjust the in-plane tension in the polyimide diaphragm (thickness $50.8 \mu\text{m}$). The diaphragm and the steel shim were preheated in an oven (Thermo Scientific, Model 6050) to a temperature T . Then, the shim was smeared with 2-h curing epoxy (FIS T120023C250) and seated on top of the diaphragm in the oven. After being heated for two hours, the diaphragm was taken out and cooled down to room temperature T_0 ($\sim 22 \text{ }^\circ\text{C}$), which generated in-plane tension in the diaphragm that was proportional to the temperature difference $\Delta T = T - T_0$ (referred to as the shrinkage temperature hereafter); see Figure 2.2b for the photo of the diaphragm.

Next, with the diaphragm attached, the shim was placed in the groove on the front endcap (see Figure 2.2a) and pressed against the housing with four screws, aligning the diaphragm with the internal cavity. A square-shaped aluminum plate ($2.3 \text{ mm} \times 2.3 \text{ mm} \times 18 \text{ }\mu\text{m}$) was glued to the diaphragm center as a reflection mirror. A cleaved optical fiber (Corning SMF-28e) was inserted into the ferrule. The distance between the fiber tip and the aluminum plate was monitored using a fiber optic interrogator (Micron Optics Si155-04-ST). When it reached $\approx 60 \text{ }\mu\text{m}$, the fiber was fixed to the ferrule using a UV-curable epoxy (Dymax OP-4-20632); see Figure 2.2c for a photo of the whole integrated device. The center displacement of the diaphragm subject to acoustic pressure stimuli was measured using a low-coherence fiber-optic interferometer (LCFOI) system (Miao Yu and Balachandran 2003), illustrated in the shaded area of Figure 2.2d. Compared with the conventional laser-based interferometer, LCFOI has one particular advantage, namely less susceptibility to wavelength and power fluctuations, which makes it ideal for measuring the displacement down to the nanometer scale or smaller. The light from a broadband superluminescent diode (SLD) (Thorlabs S5FC1018S, center wavelength 1310 nm, 40 BW, 30 mW) was delivered via a 1×2 fiber-optic coupler (Gould Fiber Optics, 50:50) to the Fabry–Pérot (FP) interferometer of the sensor head (i.e., the sensing interferometer). The reflected light was then sent to an FP-tunable filter (Micron Optics FFP-TF2, as the reference interferometer) via the same 1×2 coupler. The output light from the tunable filter was coupled into the photodetector (Newport, model 2011) and converted into an electric signal. For the whole measurement system shown in Figure 2.2d, a half-inch condenser

microphone (Brüel & Kjær, model 4191) was used as a reference sensor, from which the input pressure could be obtained. A data acquisition card (DAQ, National Instruments, model USB-6366) was connected to a computer to output the sound stimulus through a speaker (Adam A8x) and to acquire the signals from the reference microphone and the fiber-optic acoustic sensor. The sampling frequency was 200 kHz, compared with the test frequency of 500 Hz–2 kHz.

To obtain the mechanical sensitivity in terms of the center displacement per unit pressure, we followed our previous method detailed in Dong et al. (Dong et al. 2019) based on the interchangeability of the sensing interferometer and the reference interferometer in an LCFOI system. When the electric output of the LCFOI system was converted to the diaphragm displacement, it could be combined with the measured pressure stimuli from the reference microphone to obtain the frequency response function, i.e., the mechanical sensitivity as a function of frequency.

2.3 Experimental Results

2.3.1 Finite Element Simulation

In the analytical model (Liu, Olson, and Yu 2014b), the thermoviscous effect of the backing air cavity was not considered. In this follow-up study, the cavity length was varied from 0.2 mm to 30 mm. For comparison, the viscous boundary layer thickness was $69.3\ \mu\text{m}$ at 1 kHz, room temperature, and standard pressure (Blackstock and Atchley 2001). To illustrate the size effect and provide a validation for the experimental

study, a FEM model was developed using the Pressure Acoustics (PA) module or the Thermoviscous Acoustics (TA) module, in combination with the acoustics–structural interaction module in COMSOL 5.3a. Note that PA is based on the Helmholtz equation where it is assumed to be lossless, while TA is based on the linearized Navier–Stokes equations where the thermoviscous effects are considered. Taking advantage of the symmetry, as shown in the FEM model (Figure 2.3a), only a 30° segment was modeled: the air cavity was meshed using second-order brick elements, the shell was meshed using quadrilateral shell elements, and the boundary layer meshes were added near the walls. The parameters for the diaphragm are listed in Table 1, which were used in the simulation and served as the nominal values for the experiments detailed. Note that the effective coefficient of thermal expansion (CTE) μ is the difference between the CTE values of the stainless shim and polyimide diaphragm ($\mu = 12.8 \times 10^{-6} \text{K}^{-1}$). For a shrinkage temperature ΔT , the in-plane tension introduced in the circular clamped diaphragm with thickness h and Young’s modulus E is $E\mu\Delta Th$, which is equal to 114 N/m for $\Delta T = 80^\circ\text{C}$.

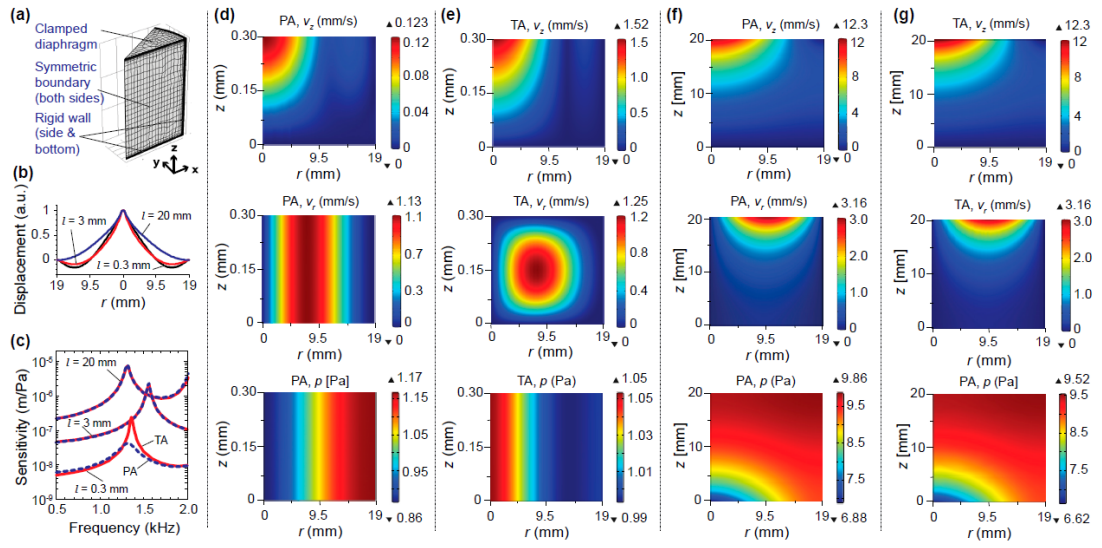


Figure 2.3: Finite element model (FEM) model and simulation results. (a) FEM model in COMSOL. (b) Mode shape (fundamental) for the three cavity lengths ($l = 0.3$ mm, 3 mm, and 20 mm) obtained using an eigenfrequency study in the COMSOL Pressure Acoustics (PA) module. (c) Mechanical sensitivity as a function of frequency for the three cavity lengths obtained using (PA, solid line) and the Thermoviscous Acoustics (TA, dashed line) module. (d–g) Field distribution of the magnitudes of the velocity in the normal/ z -direction (top), the velocity in the tangential/radial direction (middle), and the acoustic pressure (bottom) for four cases: (d): PA, $l = 0.3$ mm; (e) TA, $l = 0.3$ mm; (f) PA, $l = 20$ mm; and (g) TA, $l = 20$ mm. The frequency for all cases in (d–g) was 1.3.

Table 2.1: Properties of the polyimide diaphragm

Young's modulus E_d	2.2 GPa
Poisson's ratio ν	0.3
Density ρ_d	1290 kg/m ³
Radius a	19 mm
Thickness h_d	50.8 μ m
Expansion temperature ΔT	80 °C
Coefficient of thermal expansion μ	12.8 \times 10 ⁻⁶ 1/K
Rayleigh damping α ($\beta=0$)	500 1/s
Point mass at the center m_n	3 mg

As shown in Figure 2.3b, the mode shape of the fundamental mode changed with the cavity length due to the acoustic–structural interaction between the diaphragm and the backing air cavity, which affected its response to external pressure stimuli. The mechanical sensitivity was obtained by carrying out a frequency-domain study in COMSOL, where a uniform pressure ($p = p_0 e^{j\omega t}$, $p_0 = 1$ Pa) was applied to the external surface of the diaphragm. The displacement of the diaphragm center was extracted to obtain the mechanical sensitivity as the frequency was swept from 500 Hz to 2 kHz for three different cavity lengths ($l = 0.3$ mm, 3 mm, and 20 mm), as shown in Figure 2.3c. As the cavity length decreased, SS_c decreased; however, f_{c1} increased first but then decreased in the short-cavity-length range. These results are consistent

with the results from the analytical model (Liu, Olson, and Yu 2014). In terms of the difference between the simulation results obtained using TA and PA, when the cavity length was long ($l = 3$ mm or 20 mm), the difference was negligible. Only when the cavity length was closer to the boundary layer thickness (e.g., $l = 0.3$ mm), there was noticeable discrepancy, particularly near the resonance where the damping effect dominated. This discrepancy was due to the nature of the underlying governing equations: only the normal velocity was compatible at the acoustics–structural interface in the PA case, whereas both normal and tangential velocities were compatible in the TA case. Figure 2.3d–g shows the velocity (normal and tangential) and pressure fields for the excitation frequency of 1.3 kHz. When the cavity length was small ($l = 0.3$ mm), the normal velocity (z-direction) had similar profiles (Figure 2.3d,e top), but the magnitude was smaller in the PA case (Figure 2.3d top) than in the TA case (Figure 2.3e top). As for the tangential velocity, it was uniform in the depth direction in the PA case (Figure 2.3d middle), whereas there were clearly boundary layers adjacent to the solid walls in the TA case (Figure 2.3e middle). As a result, there were significant differences in their pressure fields (Figure 2.3d,e bottom). When the cavity length was long ($l = 20$ mm) and much larger than the boundary layer thickness, the difference was negligible, as evidenced by the similarity of the velocity and pressure fields shown in Figure 2.3f,g. To ensure consistency, the COMSOL TA simulation was used for comparison with the experimental results in the next section.

2.3.2 Experimental Verification

The device and the FEM model of the previous section were used to parametrically study the effects of the air cavity on the performances (sensitivity and natural frequency) of acoustic pressure sensors. Figure 2.4a–d shows the measured dynamic mechanical sensitivity s_{dyn} of the center diaphragm displacement in response to acoustic pressure stimuli as a function of frequency f when l decreased from 20 mm to 10 mm, 0.8 mm, and 0.3 mm, along with the FEM simulation results. For simplicity, the mechanical sensitivity can be approximated as a function of frequency f via an equivalent single-degree-of-freedom system as:

$$s_{dyn}(f) = \frac{SS_c}{\sqrt{[1-(f/f_{c1})^2]^2 + [2\xi(f/f_{c1})]^2}} \quad (1)$$

where ξ is the damping ratio. The measured and simulated sensitivity data can be curve-fitted to extract SS_c , f_{c1} , and ξ , which are shown in Figure 2.4e-g as a function of l .

As shown in Figure 2.4e, the mechanical sensitivity SS_c increased with increasing cavity length due to the stiffness effect (i.e., the longer the length, the softer the cavity), and asymptotically approached the value $1/k_d$ in vacuo (i.e., when the effects of the backing air cavity were neglected), where k_d is the effective stiffness of the diaphragm. The stiffness due to the air cavity alone k_a can be calculated from the adiabatic process as $k_a = l/(\eta\gamma p_0)$, where η is a factor to account for the non-

uniform deflection of the diaphragm contributing to the change of air volume η can be calculated using $\eta = \int_{r=0}^a u_s(r)2\pi r dr / [u_s(r=0)\pi a^2]$, where $u_s(r)$ is the static deflection of the diaphragm under uniform pressure ($\eta = 0.33$ for the circular clamped diaphragm). Combining the above two yields the sensitivity of the air-backed diaphragm $SS_c = 1/(k_d + k_a)$, as indicated by the three curves in Figure 2.4e top. In other words, the measured static sensitivity was consistent with the theory that the stiffness of the air-backed diaphragm is the sum of those of the diaphragm in vacuo and the air cavity. The bottom of Figure 2.4e shows the slope of SS_c with respect to l , which starts from an almost constant value and then asymptotically decreased to zero.

Different from the monotonic relationship between SS_c and l , the fundamental natural frequency f_{c1} showed a three-stage trend as the cavity length decreased (as shown in Figure 2.4f top): it increased in the long-cavity-length range, reached a plateau value in the medium-cavity-length range, and decreased in the short-cavity-length range. The slope shown in the bottom of Figure 2.4f shows a sign change at the cavity length indicated by the arrow, corresponding to the maximum f_{c1} . As derived in Liu et al. (Liu, Olson, and Yu 2014b), the behavior of an air-backed diaphragm in the short-cavity-length range can be modeled using two air modes and two diaphragm modes. The effects of the first and second air modes are to increase the stiffness and mass, respectively, both of which scale with $1/l$. The fundamental mode of the air-backed diaphragm can be considered a hybridization of the two modes. As l decreases, the air cavity becomes stiffer, and the contribution from the second mode increases. The

analytical derivation further shows that f_{c1} scales with \sqrt{l} in the short cavity length range, which explains the trend in Figure 2.4f for $l < 1$ mm.

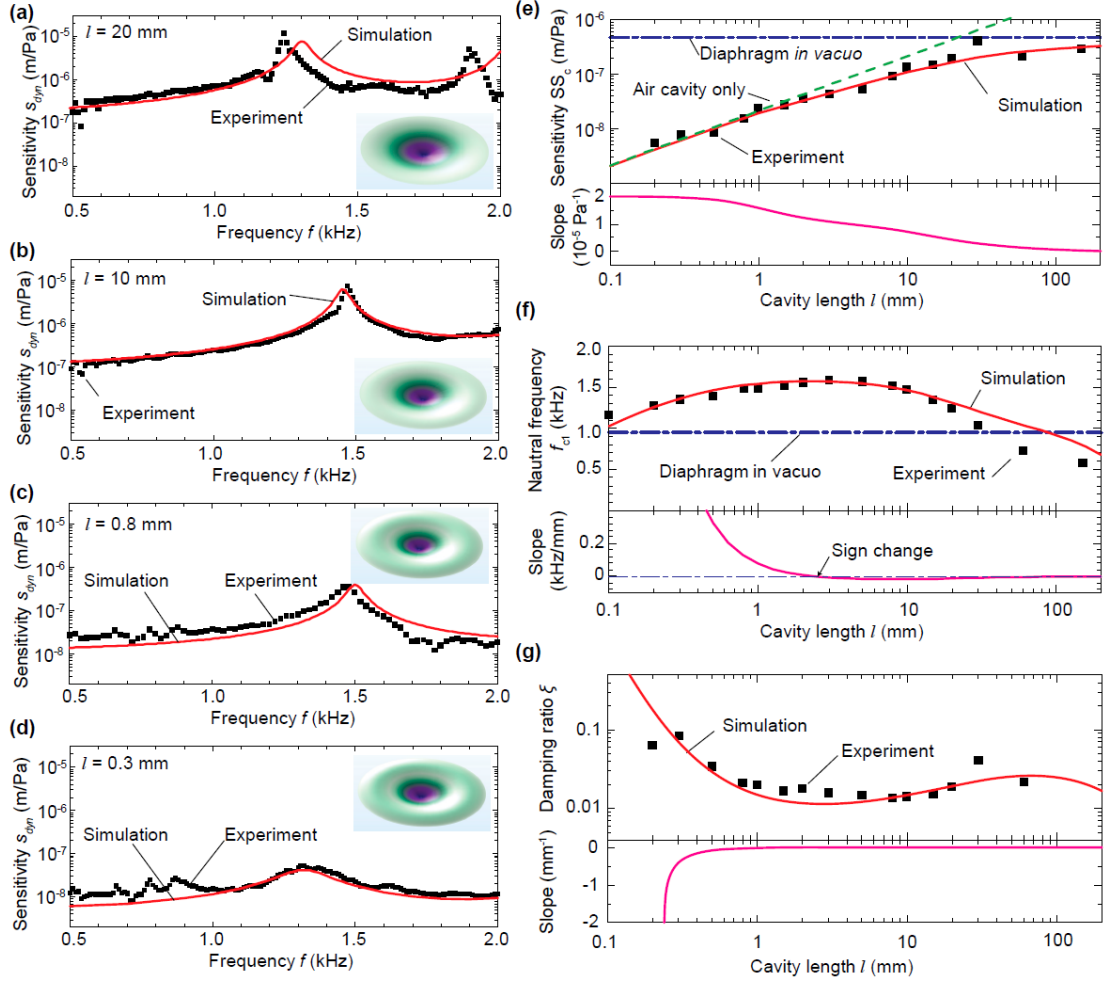


Figure 2.4 Experimental results in comparison with the simulations. (a–d): Frequency response function (i.e., mechanical sensitivity as a function of frequency) for different cavity lengths ($l = 20$ mm, 10 mm, 0.8 mm, and 0.3 mm), where the simulation results were obtained using the COMSOL Thermoviscous Acoustics module. The insets show the mode shapes for the fundamental mode. (e–g): mechanical sensitivity

(e), natural frequency (f), and damping ratio (g) as a function of cavity length. The curves in the bottom of (e–g) show the slopes

The overall trend of how the damping ratio changes with cavity length is opposite to that of the natural frequency with some exceptions. In the very short cavity length range ($l < 0.2$ mm), as indicated by the simulation data in Figure 2.3, the damping ratio increases sharply due to the enhanced viscous damping as the cavity length decreases. In the long cavity length range ($l > \approx 80$ mm), the damping ratio starts to drop as the cavity length increases. This is due to the fact that the fundamental mode in this range is an acoustic mode. Note that for dynamic pressure sensors, damping can be tuned post-fabrication by changing the design of the hole plate underneath the diaphragm (Homentcovschi and Miles 2005; Bao et al. 2003). As such the focus of this section is on the sensor sensitivity and the fundamental natural frequency, which are the two important metrics in sensor design.

A parametric study is further carried out to validate the above finding when the in-plane tension is varied by changing the shrinkage temperature ΔT from 70 °C to 130 °C (the corresponding in-plane tension varies from 100 N/m to 186 N/m). As shown in Figure 2.4a-d, both sensitivity SS_c and the fundamental natural frequency f_{c1} are plotted as a function of the air cavity length l and shrinkage temperature ΔT . Overall, there is a good agreement between the experiment and simulation results, and similar three-stage trends in terms of the effect of cavity length are observed for all tested values of ΔT ,

validating the results in the analytical model (Liu, Olson, and Yu 2014). In the studied cavity length range, the air cavity is much stiffer than the diaphragm. As such, for a fixed cavity length, increasing ΔT will increase the stiffness of diaphragm *in vacuo*, but the stiffness of air-backed diaphragm is largely unchanged, as shown in Figure 2.5c for three representative values of l (0.5 mm, 2 mm, and 20 mm). However, increasing ΔT will increase the fundamental frequency f_{c1} , as shown in Figure 2.5 for the same values of l . As discussed in Liu et al. (Liu, Olson, and Yu 2014b), the plateau frequency in the medium cavity length range is between the first and second natural frequencies f_{d1} and f_{d2} of the diaphragm *in vacuo*. As shown in Figure 2.5g, when the in-plane tension increases, both f_{d1} and f_{d2} increase. As a result, f_{c1} of the air-backed diaphragm increases accordingly.

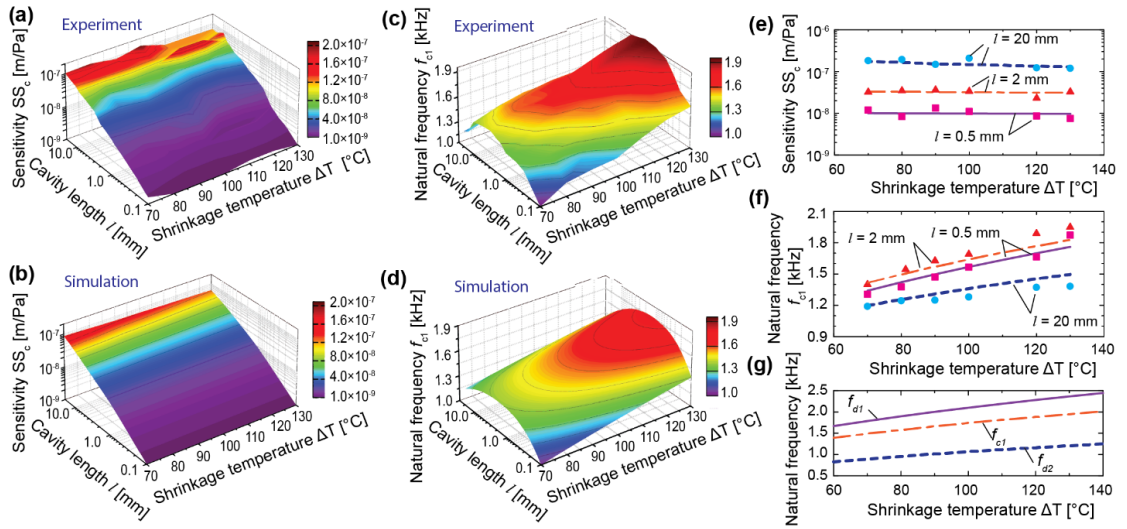


Figure 2.5 Parametric study by changing the in-plane tension in the diaphragm via thermal expansion and cooling: (a,b) Contour plot of sensitivity as a function of cavity

length l and shrinkage temperature ΔT (top (a): experiment, bottom (b): simulation (b)). (c,d): same as (a,b) but for the natural frequency; (e,f): Mechanical sensitivity (e) and natural frequency (f) as a function of ΔT for three different cavity lengths 0.5 mm, 2 mm, and 20 mm (scatter points: experiment, lines: simulation). (g) Natural frequencies of the first two modes of the diaphragm *in vacuo* (denoted as f_{d1} and f_{d2}) and the first fundamental frequency of air-backed diaphragm with $l = 2$ mm, denoted as f_{c1} .

The discrepancy between the experimental data and simulation results can be attributed to several factors. The first is the nonlinearity and hysteresis of the tunable filter of the optical detection system when a bias voltage is applied to the reference filter. Second, although the testing is conducted in a room with absorbing foams on the sidewalls and ceiling, it is not an anechoic chamber; there are some unwanted echoes during the testing. The third is the variation of the point mass added to the diaphragm center. Lastly, the thermal stress in the diaphragm may not be consistently controlled due to the fluctuation of room temperature and relaxation of the diaphragm.

2.4 Summary

A comprehensive experimental study was carried out to systemically investigate how the diaphragm in a dynamic pressure sensor interacts with the backing air cavity and affects the sensor performance. Large-scale dynamic pressure sensors using circular clamped polyimide diaphragms were fabricated and characterized when the length of the backing cavity and the in-plane tension in the diaphragm were varied. The

experimental results compared well with the FEM simulations and validated the previous findings from the analytical model (Liu, Olson, and Yu 2014b) on the static mechanical sensitivity and the fundamental natural frequency f_{c1} . As the cavity length l decreased, SS_c decreased monotonically. When l was below a critical value, the stiffness of the air cavity dominated that of the diaphragm. For f_{c1} , it showed a three-stage trend as l decreased: increasing in the long-cavity-length range, reaching a plateau value in the medium-cavity-length range, and decreasing in the short-cavity-length range.

These experimentally validated findings have a profound implication on how to model a simple yet common structure of an air-backed diaphragm. Traditionally, the backing air cavity has been modeled as an effective spring element k_a , as taught in acoustics (Beranek 1954) or sensor design (Antonsson and Cagan 2001) textbooks. However, this approach of modeling cannot capture the full acoustics–structural interaction between the diaphragm and the backing air cavity correctly, particularly when the cavity length is very short. The traditional lumped model will always predict an increased fundamental natural frequency as the cavity length becomes shorter. However, as demonstrated in this chapter, the interaction is more complex. The backing air cavity affected both the effective stiffness and mass of the diaphragm. Shorter air cavity resulted in larger k_a and thus increased the diaphragm’s effective stiffness. A shorter air cavity also increased the effective mass, although the total mass of the air enclosed in the cavity was smaller. The combination of these two effects led to a counterintuitive

phenomenon in the short-cavity-length range where a shorter cavity length caused the fundamental natural frequency to decrease.

These findings also serve as important guidelines for practically designing dynamic pressure sensors, particularly for miniaturized sensors where the cavity must be made short to reduce the overall sensor size. If the configuration is a uniform circular clamped diaphragm backed by a cylindrical air cavity, the formula provided in Liu et al. (Liu, Olson, and Yu 2014b) would be useful to determine whether the cavity length falls within the long-, medium-, or short-cavity-length regimes, and estimate the sensitivity and fundamental natural frequency. For more complex configurations, FEM simulations can be used to guide the sensor design.

Research outcome:

Dong, Qian, Xiaolei Song, and Haijun Liu. "Effects of Air Cavity in Dynamic Pressure Sensors: Experimental Validation." *Sensors* 20.6 (2020): 1759.

CHAPTER 3: MINIATURE DYNAMIC PRESSURE SENSORS WITH A GRAPHENE DIAPHRAGM

3.1 Introduction

Graphene has been known to possess exceptional mechanical properties, including its extremely high Young's modulus and atomic layer thickness. Although there are several reported fiber optic pressure sensors using graphene film, a key question that is not well understood is how the suspended graphene film interacts with the backing air cavity and affects the sensor performance. Based on our previous analytical model (Liu, Olson, and Yu 2014b), we will show that the sensor performance suffers due to the significantly reduced mechanical sensitivity by the backing cavity. To remedy this limitation, we will, through experimental and numerical methods, investigate two approaches to enhance the sensitivity of fiber optic acoustic pressure sensors using graphene films. First, a graphene–silver composite diaphragm is used to enhance the optical sensitivity by increasing the reflectivity. Compared with a sensor with pure graphene diaphragm, graphene–silver composite can enhance the sensitivity by threefold, while the mechanical sensitivity is largely unchanged. Second, a fiber optic sensor is developed with enlarged backing air volume through the gap between an optical fiber and a silica capillary tube. Experimental results show that the mechanical sensitivity is increased by $10\times$ from the case where the gap side space is filled. For both approaches, signal-to-noise ratio (SNR) is improved due to the enhanced sensitivity, and COMSOL Thermoviscous acoustics simulation compares well with the experimental results. This study is expected to not only enhance the understanding of

fluid–structural interaction in sensor design but also benefit various applications requiring high-performance miniature acoustic sensors.

Graphene, a single atomic layer of carbon arranged in a regular hexagonal pattern, has been demonstrated to possess exceptional mechanical (Lee et al. 2008), thermal (Balandin et al. 2008), electronic (Castro Neto et al. 2009), and chemical (Loh et al. 2010) properties since its discovery in the free state (Novoselov, Jiang, et al. 2005; Novoselov et al. 2004; Novoselov, Geim, et al. 2005). For a monolayer graphene with a thickness of 0.34 nm, its Young's modulus reaches 1 TPa, establishing graphene the strongest material ever measured (Lee et al. 2008). It is also known that graphene can endure a large deformation of up to 20%. Further, graphene can survive at a temperature as high as 700 °C (Kahng et al. 2012; Kim et al. 2010).

Thanks to the recent development on the fabrication of large-area graphene by mechanical exfoliation (Hernandez et al. 2008; Novoselov et al. 2004) or chemical vapor deposition (CVD) (X. Li, Cai, et al. 2009; Reina et al. 2009) and the techniques of transferring it to a different substrate (X.-D. Chen et al. 2013; X. Li, Zhu, et al. 2009; Lock et al. 2012; Suk et al. 2011), fruitful progress has been made to not only better understand the graphene material but also explore its use in a variety of applications (Geim 2009; Geim and Novoselov 2007). Examples include high speed transistors with high carrier mobility and large saturation velocity (Y-M Lin et al. 2010; Yu-Ming Lin et al. 2011) and bio-sensors having large surface areas and high electrical conductivity (Kuila et al. 2011). While most research efforts thus far have been focused on the

electronic properties of graphene (e.g., the application of graphene for gas sensors (Schedin et al. 2007; Hill, Vijayaraghavan, and Novoselov 2011; Basu and Bhattacharyya 2012)), a few endeavors have been attempted to directly take advantage of its unique mechanical properties (A. D. Smith et al. 2013; J. Ma et al. 2012; 2013; C. Li et al. 2014). In one study, a suspended graphene film was exploited as both the pressure transducer and the electrical signal readout element, whose resistance changes with the applied pressure on the film (A. D. Smith et al. 2013). In another study, a low finesse Fabry-Pérot (FP) interferometer was constructed using a few-layer graphene covering a fused silica capillary tube which is spliced to the tip of an optical fiber (J. Ma et al. 2012). With a diaphragm diameter of 25 μm and cavity length of 21 μm , this graphene-based pressure sensor demonstrated a pressure sensitivity of 39.4 nm/kPa when it was calibrated using static pressure to the range of ~ 10 kPa. Targeting the audible frequency range, a fiber optic acoustic sensor with a 100 nm thick graphene film covering the end surface of a ceramic ferrule (with a typical outer diameter of 1.25 mm) was demonstrated (J. Ma et al. 2013). In a following study, the same system configuration was used, but the sensor diaphragm was changed to a 13-layer graphene film (C. Li et al. 2014).

In the development of dynamic pressure sensors, the graphene's unique combination of exceptional high Young's modulus and thickness down to atomic layers is theoretically advantageous for developing sensors with unprecedented performance despite the trade-off between bandwidth and sensitivity. For a dynamic pressure sensor with a

clamped circular diaphragm, as illustrated in Figure 3.1a, the fundamental natural frequency f_1 is given by (Ventsel and Krauthammer 2001)

$$f_1 = \frac{2.95}{2\pi} \frac{h}{a^2} \sqrt{\frac{E}{\rho(1-\nu^2)}} \quad (2)$$

where E , ν , ρ , a , and h are the Young's modulus, Poisson's ratio, density, radius, and thickness of the diaphragm, respectively. Here the in-plane tension is assumed to be zero for ease of comparison. Note that the fundamental natural frequency largely determines the sensor bandwidth (de Silva 2016), although the damping also plays a role. On the other hand, the static mechanical sensitivity of the sensor can be calculated by (Ventsel and Krauthammer 2001):

$$S_{M0} = \frac{3(1-\nu^2)}{16E} \frac{a^4}{h^3} \quad (3)$$

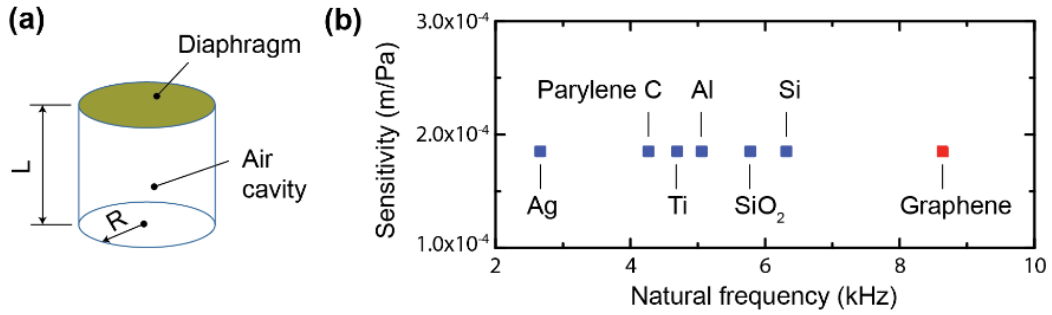


Figure 3.1 Air-backed diaphragms for acoustic pressure sensors. (a) Schematic of a circular clamped diaphragm backed by a cylindrical air cavity with rigid side and bottom walls; (b) natural frequencies of using different materials to achieve the same

sensitivity without considering the effect of the backing cavity ($L = 67 \mu\text{m}$, $R = 40 \mu\text{m}$).

According to Eqs. ($f_1 = \frac{2.95}{2\pi} \frac{h}{a^2} \sqrt{\frac{E}{\rho(1-\nu^2)}}$) and ($S_{M0} = \frac{3(1-\nu^2)}{16E} \frac{a^4}{h^3}$), in order to achieve a high natural frequency f_1 , which usually leads to a large sensor bandwidth, it is more favorable to design a sensor with a smaller radius, a larger thickness, or choose a material with a higher Young's modulus, all of which will result in a decreased sensitivity S_{M0} , thus the so-called trade-off between bandwidth and sensitivity.

To compare the performance of sensors made of different materials, the diameter of the circular clamped diaphragm is fixed at $80 \mu\text{m}$, the diaphragm thickness is varied to achieve the same sensitivity. For the graphene film of 4-monolayer thick, the equivalent material parameters are chosen as $E = 1 \text{ TPa}$, $\nu = 0.17$, and $\rho = 2,200 \text{ kg/m}^3$ (Poot and van der Zant 2008; Lee et al. 2008). As shown in Figure 3.1b and Table 2 (columns for the “without air cavity” case), the sensor with a thin graphene diaphragm exhibits a much higher natural frequency for the same static sensitivity. This result can be understood by examining the scaling in Eqs. ($f_1 = \frac{2.95}{2\pi} \frac{h}{a^2} \sqrt{\frac{E}{\rho(1-\nu^2)}}$) and ($S_{M0} = \frac{3(1-\nu^2)}{16E} \frac{a^4}{h^3}$): f_1 scales with $hE^{1/2}$ while S_{M0} scales with $h^{-3}E^{-1}$. Therefore, in order to achieve a higher natural frequency but keep the same static sensitivity, one can choose a material with a higher Young's modulus and at the same time reduce the diaphragm thickness. For example, if a material with a Young's modulus of 8 times

larger is chosen, the thickness can be reduced by half to obtain the same sensitivity, which yields a natural frequency that is more than 40% higher. This explains the advantage of graphene having an extremely high Young's modulus and small thickness.

However, according to our previous theoretical study on the acoustic-structural interaction of air-backed diaphragms (Liu, Olson, and Yu 2014b), the air cavity backing the diaphragm plays a critical role in determining the sensor performance, particularly for miniature sensors with small air cavity. To accurately predict the sensor performance, the acoustic-structural interaction between the diaphragm and the backing air cavity has to be taken into account. Using the developed continuum mechanics model, the sensitivity and fundamental natural frequency of the air-backed graphene are calculated as $S_{M0} = 1.42 \text{ nm/Pa}$ and $f_1 = 14.0 \text{ kHz}$, respectively. In other words, the backing air cavity reduces the mechanical static sensitivity by more than five orders of magnitude while increasing the natural frequency by 62%. This demonstrates why it is critical to consider the effects of air cavity in small transducers. As shown Table 2 (columns for the "with air cavity" case), since the sensitivity is largely limited by the air cavity, the thickness for other materials can be simply varied to achieve the same sensitivity and fundamental natural frequency as the graphene.

Table 3.1: Comparison of properties and performance of different diaphragm materials for acoustic sensors

Material	Material properties			Without air cavity			With air cavity		
	E (GPa)	ν	ρ (Mg/m ³)	h (nm)	S_{M0} ($\mu\text{m}/\text{Pa}$)	f_1 (kHz)	h (nm)	S_{M0} (nm/Pa)	f_1 (kHz)
Silver	83	0.37	10.5	3.00	185	2.66	5.03	1.42	14.0
Parylene C	4.5	0.4	1.29	7.85	185	4.70	9.35	1.42	14.0
Titanium	110	0.32	4.43	2.76	185	4.26	3.43	1.42	14.0
Aluminum	69	0.32	2.7	3.23	185	5.06	3.72	1.42	14.0
Silicon dioxide	90	0.17	2.2	3.04	185	5.78	3.33	1.42	14.0
Silicon	169	0.25	2.3	2.43	185	6.31	2.59	1.42	14.0
Graphene	1000	0.17	2.2	1.36	185	8.63	1.36	1.42	14.0

Note: The simulation results for a circular clamped diaphragm with a diameter of 80 μm . The cylindrical air cavity has the same diameter as that of the diaphragm and a length of 67 μm . The thickness in the “without air cavity” case is varied to obtain the same mechanical sensitivity for different materials. In the case of “with air cavity”, since the mechanical sensitivity is limited by the much stiffer backing air cavity, the thickness is varied to obtain same natural frequency for different materials.

Given the limitation on the mechanical sensitivity by the backing air cavity, the goal of this paper is to explore different ways to enhance the sensitivity of graphene-based fiber optic acoustic pressure sensors. The sensor's ultimate sensitivity S_T can be considered as the product of mechanical sensitivity S_M (transduction from pressure stimulus to mechanical displacement) and optical sensitivity S_O (transduction from mechanical displacement to electric voltage output), i.e., $S_T = S_M S_O$. Targeting one of these two transduction stages, one approach is to use the graphene-silver composite as the diaphragm material with the goal of enhancing the optical reflectivity to achieve higher optical sensitivity S_O ; the other approach is to create a larger backing cavity with the goal of increasing the mechanical sensitivity S_M . These two approaches are detailed in the following sections, along with a section of discussion.

3.2 Fiber Optic Sensors with Graphene-Silver Composite Diaphragms

3.2.1 Fabrication

The schematic of the sensor is shown in the inset of Figure 3.2a. The main structure of the sensor is an ultraviolet (UV)-molded polymer cavity covered with a graphene-silver composite diaphragm, which forms a FP interferometer between the diaphragm and the fiber end face. The fabrication process of the polymer cavity is illustrated in Figure 3.2b. The first step is to construct a fiber-based mold by inserting a cleaved fiber (80 μm for the cladding diameter) into a zirconia ferrule with the fiber protruding about 67 μm and permanently fixing the fiber with a UV-light-curable polymer (Dymax OP-54), following an approach detailed in reference (Bae and Yu 2012) (step i). The polymer

completely filled the gap between the ferrule and the 80 μm fiber due to the capillary force and low viscosity. The fabricated mold is then cleaned and treated with an organosilane (Gelest methacryloxypropyltrimethoxysilane, SIM6487.4) to facilitate the releasing in the molding process. The second step is to dispense a small drop of UV-curable polymer (Dymax OP-4-20632) on another cleaved optical fiber (Corning SMF-28) used as part of the sensor by using a separate fiber placed in the middle of the mold. The sensor fiber is aligned with the mold by coupling light through the fiber and monitoring the intensity exiting the fiber and received by the mold fiber. By adjusting the relative position of the sensor fiber to the mold, a desirable alignment can be achieved when the maximal transmitted intensity is obtained. Further, the polymer is pre-cured by using a UV light source (Hamamatsu, LC5) for 12 seconds at 12% intensity, followed by releasing the mold to obtain the molded cavity (diameter of 80 μm and depth of 67 μm). Finally, the polymer cavity is post-cured by using a spot UV light source (Dymax, BlueWave 50AS) for 100 seconds and baked on a hot plate (150 $^{\circ}\text{C}$) for three hours to enhance the thermal stability.

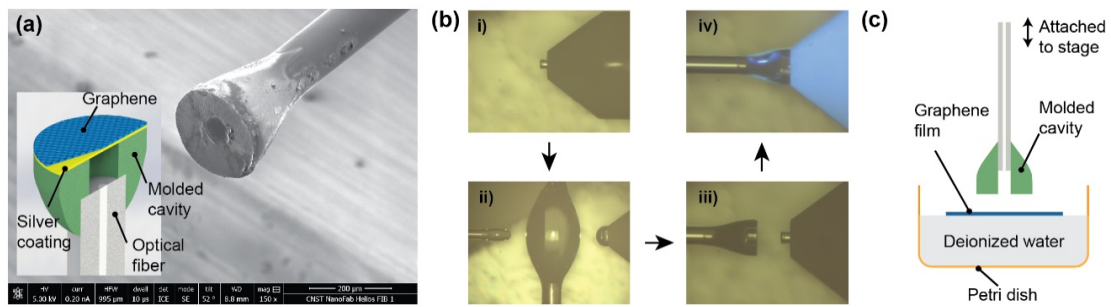


Figure 3.2 Ultraviolet-molded fiber optic sensors with graphene (or graphene-silver composite) diaphragms. (a) SEM image of the sensor with its schematic shown in the inset; (b) fabrication process of the molded cavity; (c) schematic of transferring graphene film onto the molded cavity.

The graphene film (purchased from GrapheneSuperMarket.com) is originally deposited via CVD on nickel, which is itself on top of a silicon substrate. The average thickness of graphene is four atomic layers. Silver of selected thickness (5 nm) is deposited on top of the graphene by using e-beam evaporation. To release the graphene-silver film from the substrate, a 0.5% FeCl_3 solution is used to etch the nickel starting from the peripherals. When the nickel is completely removed, the released graphene film floats on top of the solution, which is then diluted by distilled water multiple times to remove the residual etchant. The released film is then transferred onto the polymer substrate by pushing down the molded cavity vertically and retreat, as illustrated in Figure 3.2c, essentially a punching process. When the top surface of the cavity is in contact with the film, the film is bonded to the polymer substrate by Van der Waals force to complete

the sensor fabrication. The scanning electron microscope (SEM) picture of the fabricated sensor is shown in Figure 3.2a.

3.2.2 Experimental Characterization

To detect the sound pressure induced diaphragm center displacement of the sensors, a low-coherence fiber optic interferometer (LCFOI) system (Miao Yu and Balachandran 2003) was used, as shown in Figure 3.3a. Compared with the conventional laser-based fiber optic interferometer, LCFOI has one particular advantage of less susceptibility to wavelength fluctuation and is thus ideal for measuring nanometer displacement or below. The light from a broadband superluminescent diode (SLD) (Thorlabs S5FC1018S, center wavelength 1310 nm, 40 BW, 30 mW) was delivered via a 1×2 fiber optic coupler (Gould Fiber Optics, 50:50) to the FP interferometer of the sensor head (i.e., the sensing interferometer). The reflected light was then sent to a FP tunable filter (Micron Optics FFP-TF2) (i.e., the reference interferometer) via the same 1×2 coupler. The output light from the tunable filter was coupled into the photodetector (New Focus, Model Velocity 2011) and converted into an electric signal, which is the voltage output of the sensor. A 1/2-inch condenser microphone (Brüel & Kjær, model 4191 with pre-amplifier 2690-0S2) was used as a reference sensor. A National Instruments data acquisition card (DAQ, model USB-6366) was connected to a computer to output the sound stimulus through a tweeter speaker (ESS AMT, pre-amplified by a SONY audio receiver STR-DH100) and to acquire the signals from the

reference microphone and the fiber optic acoustic sensor. The incident angle is 0° , i.e., the sensor front points toward the speaker.

In order for the LCFOI system shown in Figure 3.3a to work properly, the optical path differences (OPD) of the sensing interferometer (i.e. the sensor head) δ_s and reference interferometer (i.e., the tunable filter) δ_r need to satisfy $\delta_s \approx \delta_r \gg l_c$ and $(\delta_s - \delta_r) \ll l_c$, where l_c is the coherence length of the SLD light source (Granttan and Meggitt 2000). Under this condition, the photodetector output I can be expressed as

$$I = I_{dc} - I_{ac} \cos[k_0(\delta_s - \delta_r)] \quad (4)$$

where k_0 is the wave number in free space, and I_{dc} and I_{ac} are two constants determined by the mirror reflectivity in the FP interferometers and the light source intensity. Note that $\delta_s - \delta_r = 2(L_s - L_r)$, where L_s and L_r are the mirror separation in each of the two FP interferometers. When the system is operated at quadrature points $k_0(\delta_s - \delta_r) = \pi/2 (2m - 1)$, where m is an integer, the LCFOI system has the maximum output in response to a dynamic change of L_s or L_r .

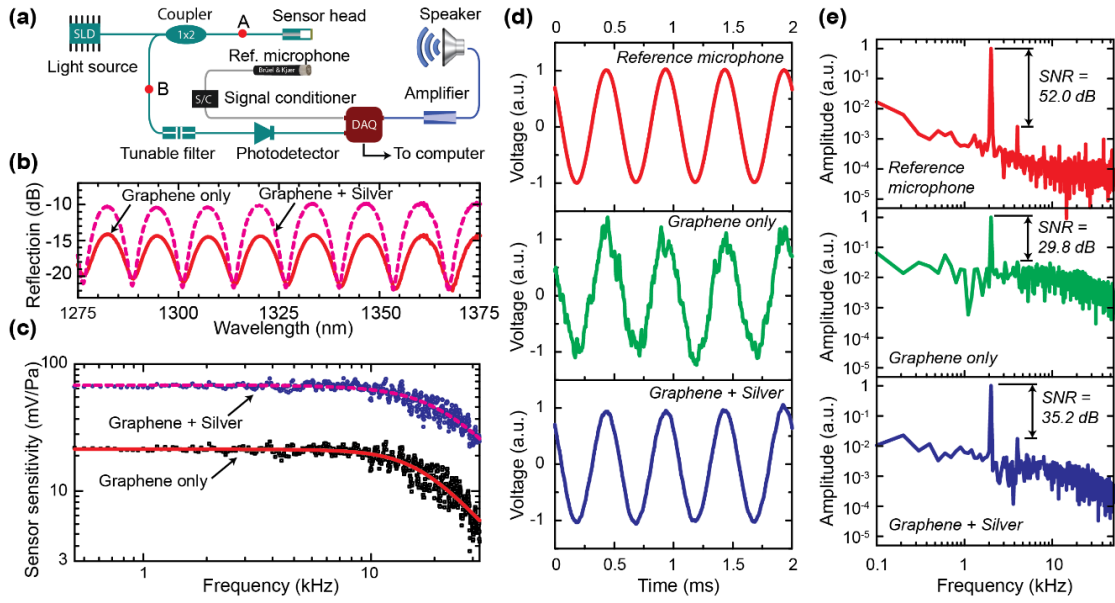


Figure 3.3 Experimental characterization of UV-molded graphene-based fiber optic sensors. (a) Experimental setup with a low coherence fiber optic interferometric system; (b) reflectivity of the Fabry-Perot interferometer of the sensor head; (c) frequency response of sensors with two different kinds of diaphragms (dots for experiments, and lines for simulation); (d) time domain signals at 2 kHz from the reference microphone (top), fiber optic sensor with graphene only as the diaphragm (middle), and sensor with graphene and silver composite diaphragm (bottom), all of which are normalized to have an amplitude of one; (e) Fourier transform of the signals in (d).

To quantify the enhancement of optical reflectivity of graphene-silver composite, the reflection spectrum of the sensor was measured by using an optical spectrum analyzer (OSA, Agilent 86142B) via two steps. First, disconnecting the FP sensor head, OSA is connected at point A in Figure 3.3a to measure the input spectrum $I_{in}(\lambda)$ to the sensor

head, where λ is the optical wavelength. Next, with the sensor head connected, OSA is inserted at point B to measure the output spectrum $I_{out}(\lambda)$. Then, the reflection function of the FP sensor head can be calculated as $R(\lambda) = 2I_{out}(\lambda)/I_{in}(\lambda)$, where the factor of two is to account for the 50:50 split ratio of the optical coupler. The measured $R(\lambda)$ is shown in Figure 3.3b (magenta dashed line) and compared with a second UV-molded sensor with a graphene-only diaphragm (red solid line). With the added silver layer, $R(\lambda)$ is enhanced on average by a factor of 2.63 (or 4.2 dB) at the peaks and reduced by a factor of 0.84 (or 0.8 dB) at the valleys. Note that the peaks/troughs of the spectra of two sensors are well aligned, indicating that the cavity length is consistent in different samples due to the nature of the UV-molding fabrication process. In short, due to the enhanced optical reflectivity of the graphene-silver composite, the reflection spectrum of the sensor with a graphene-silver composite diaphragm exhibits a $\sim 3x$ reflectivity enhancement compared with that of the sensor with a pure graphene diaphragm.

To characterize the performance of the sensors, frequency sweep was carried out to obtain their frequency response, as shown in Figure 3.3c. Note that the sensitivity frequency response $S_T(f)$ in terms of photodetector output per unit pressure stimulus can be approximated by a lumped model as a function of excitation frequency f :

$$S_T(f) = \frac{S_{T0}}{\sqrt{(1-(f/f_1)^2)^2 + (2\zeta(f/f_1))^2}} \quad (5)$$

where S_{T0} is the sensitivity extrapolated to $f = 0$, f_1 is the fundamental natural frequency, and ζ is the damping ratio. The values of S_{T0} , f_1 , and ζ can be obtained through least squares fitting, as listed in Table 3.

Table 3.2: Effects of silver on graphene-based acoustic sensors

	Graphene only		Graphene + Silver	
	Nominal	Uncertainty*	Nominal	Uncertainty*
Sensor sensitivity S_{T0} (mV/Pa)	21.32	0.39	68.41	1.00
Natural frequency f_1 (kHz)	16.18	0.46	20.22	0.71
Damping ratio ζ	0.73	0.03	0.79	0.03
Mechanical sensitivity (nm/Pa)	1.55	0.03	1.17	0.02

*: Expanded uncertainty using coverage factor $k = 2$

To obtain the mechanical sensitivity S_M , an electrical sinusoidal voltage is applied to the reference interferometer (i.e., the FP tunable filter), which has a calibrated sensitivity of phase change to the voltage modulation (69.7 nm/V). Since the reference interferometer and the FP sensing interferometer are interchangeable, the phase change of the sensing interferometer due to the sound stimulus is equivalent to applying a sinusoidal modulation signal to obtain the same phase change from the tunable filter without the sound stimulus. By using this method, the mechanical sensitivity was

calibrated to be 1.55 nm/Pa and 1.17 nm/Pa for the sensors without silver layer and with 5 nm-thick silver layer, respectively.

As can be seen from Figure 3.3c and Table 3, the most prominent effect of adding the silver coating is that the optical sensitivity of the sensor is improved three-fold. However, the mechanical sensitivity is largely unchanged, which confirms that the improved sensor sensitivity is mostly due to the enhanced optical reflectivity of the diaphragm. Furthermore, the natural frequency is also slightly improved (from 16.2 kHz to 20.2 kHz), but the damping ratio almost remains the same (from 0.73 to 0.79). At a specific frequency (e.g., 2 kHz), the two fiber optic acoustic sensors are compared against the reference microphone in both time domain (Figure 3.3d) and frequency domain (Figure 3.3e). The waveform amplitudes are normalized to one for ease of comparison. It can be seen that the addition of silver of a few nanometers results in much cleaner signals in time domain and overall better signal-to-noise ratio (SNR) in frequency domain, an improvement of 5.4 dB (from 29.8 dB to 35.2 dB).

To compare the repeatability of the developed sensors against the reference microphone, we define the normalized error (NE) as $NE(\%) = (V_{\max} - V_{\min})/V_{\text{avg}} * 100$, where V_{\max} , V_{\min} and V_{avg} are the maximum, minimum, and average amplitudes, respectively, of three measurements for frequencies between 500 Hz and 20 kHz. For the fiber optic sensor with graphene-only diaphragm, NE has a mean of 0.78% for the reference microphone and 1.77% for the fiber optic sensor, a ratio of 2.27 (=

1.77%/0.78%). With the added silver layer to enhance the optical sensitivity, this ratio is improved to 1.59 (= 1.34%/0.84%).

3.3 Finite Element Simulation

In our previously analytical model (Liu, Olson, and Yu 2014b), the medium (air) is assumed to be lossless and only the normal velocity is compatible at the fluid-structural interface. This prevents its application for miniature fiber optic sensors where the domain size is comparable to the thermal/viscous boundary layer thickness. For example, the thermal boundary layer thickness is 49 μm at 2 kHz; the diameter and length of the cylindrical backing air cavity are 80 μm and 67 μm , respectively. To better understand the mechanical behavior of the fabricated sensors, a finite element method (FEM) model, shown in Figure 3.4 a, is developed using COMSOL Thermoacoustic Acoustics, where the air domain is described using Navier-Stokes equations and meshed using brick second-order elements, and the diaphragm is meshed using quadrilateral second-order shell elements. At the interface, both normal and tangential velocities are assumed to be compatible and boundary layer meshes are added for each sweep frequency. In comparison, the same model can be solved using COMSOL Pressure Acoustics, similar to our analytical model (Liu, Olson, and Yu 2014), where it is assumed to be lossless in air and the tangential compatibility constraint is relaxed.

The material properties listed in Table 2 for graphene and silver are used in the simulation. For the graphene–silver bilayer composite diaphragm, the total thickness

(6.36 nm) is the sum of graphene and silver, the density (8725 kg/m³) and Poisson's ratio (0.33) are the weighted sum by the thickness, and the effective Young's modulus (50.7 GPa) is calculated by using the equivalent bending stiffness (Hou and Chen 2004).

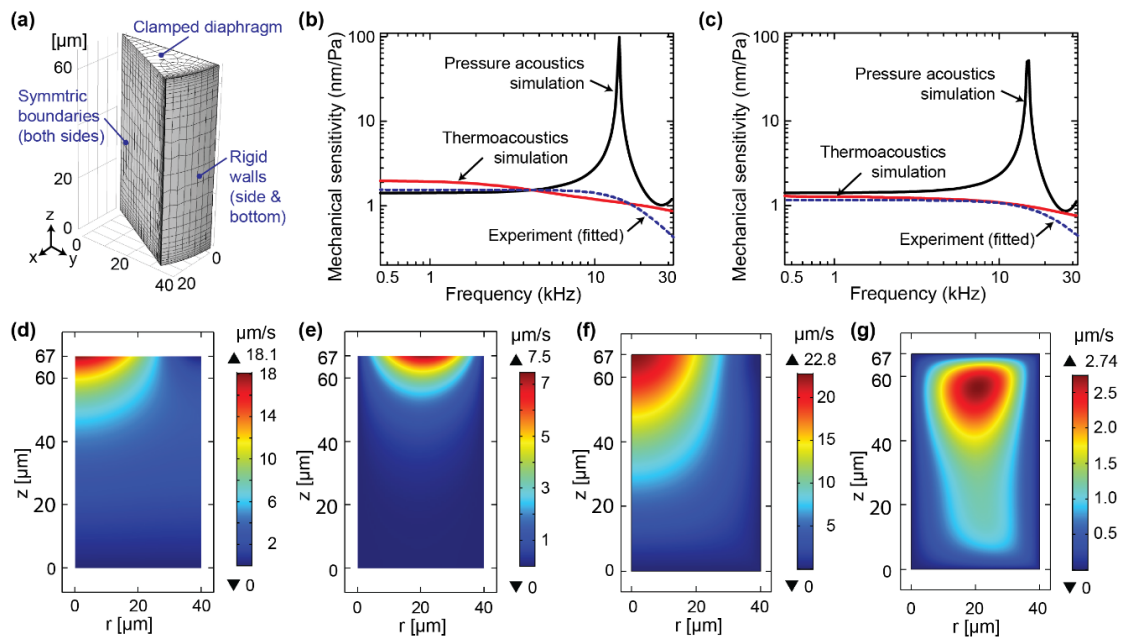


Figure 3.4 Numerical simulation to obtain the frequency response for the fabricated fiber optic sensors using COMSOL. (a): FEM model using COMSOL Multiphysics; (b)&(c): mechanical sensitivity as a function of frequency, comparing two kinds of FEM simulations with the experiment results, for the sensors with graphene-only (b) and graphene-silver composite (c) films; (d)-(e): cross-section views of velocity fields (normal (d) and tangential (e)) for the fiber optic sensor with graphene-only diaphragm at 2 kHz, obtained using pressure acoustics simulation in COMSOL where loss is neglected; (f)-(g): velocity fields (normal (f) and tangential (g)) for the same sensor and

same frequency as in (d)-(e) but obtained using thermoacoustics simulation in COMSOL where thermal and viscous losses are considered.

As shown in Figure 3.4b-c, the thermoacoustic simulation has an overall much better agreement with the experimental measurements. The difference between the lossless Pressure Acoustics simulation and lossy Thermoacoustics can be seen from the contour plots for the normal and tangential velocities for sound frequency 2 kHz (Figure 3.4d-g). In particular, the normal velocity field is excited deeper into the backing air domain in thermoacoustics simulation (Figure 3.4f) than in pressure acoustic simulation (Figure 3.4d). The maximum tangential velocity occurs at the interface in Pressure Acoustics simulation (Figure 3.4e), while it is about 10 μm from the interface in Thermoacoustic simulation (Figure 3.4g). As a result, there is significant difference in the damping characteristics of the sensor, and slight difference in the simulated sensitivity. For example, at sound frequency of 2 kHz, the simulated mechanical sensitivity for the graphene-only sensor is 1.44 nm/Pa using Pressure Acoustics and 1.81 nm/Pa using Thermoacoustics, as opposed to measured value 1.55 nm/Pa; for the sensor with graphene-silver film, it is 1.44 nm/Pa using Pressure Acoustics and 1.25 nm/Pa using Thermoacoustics, as opposed to the measured value of 1.16 nm/Pa. The discrepancy between the simulation and experimental results can be attributed to a number of factors, including the nonlinearity and hysteresis of the tunable filter when applying a bias to tune the cavity length, the non-ideal lab environment for sound testing since it is not an

anechoic chamber, non-negligible tension in the diaphragm, and the inaccurate material properties used in the simulation.

3.4 Fiber Optic Sensors with Graphene Diaphragm and Enlarged Backing Air Cavity

The second approach to improve the sensor sensitivity is to increase the mechanical sensitivity by enlarging the backing air cavity while not compromising the optical sensitivity. As shown in the schematic (Figure 3.5a), the main structure of the sensor consists of an optic fiber (Corning SMF-28, 125 μm in diameter) inside a silica capillary tube (Polymicro TSP150375), which has an inside diameter of 147 μm and outside diameter of 323 μm . Although the distance between the fiber tip and the graphene diaphragm is kept at 57 μm , the extra side gap space between the fiber and the capillary tube has a volume of 0.046 mm^3 . This volume divided by the inside diameter of the tube gives an equivalent cavity length of 2.7 mm, which is 47 times the distance between the fiber end face and graphene film.

The experimental characterization and simulation process are exactly same as in previous section, except that a different light source (Thorlabs S5FC1005S), tunable filter (Micron Optics FFP-TF), and speaker (Adam A8x) are used. The details are thus omitted for brevity.

3.4.1 Fabrication Process

The first step is to cut the capillary tube to the desired length, remove the polymer coating on one end, and polish the end face. Next, the graphene film is transferred onto the polished end of capillary tube using the previously described punching process (see Figure 3.5b for the SEM picture after this step). Then, a cleaved optical fiber is inserted from the back side into the capillary tube to the desired distance, which is verified by a fiber optical interrogator (Micron Optics SI155-04-ST). Lastly, to enclose the opening and fix the optical fiber, a low-shrinkage UV-curable polymer (DYMAX OP-61-LS) is added and cured using a spot UV light source (DYMAX Blue Wave LED Prime UVA).

The measured mechanical sensitivity is shown as a function of frequency in Figure 3.5c, along with simulated results using COMSOL Thermoacoustics. The measured mechanical sensitivity is 6-10 nm/Pa in the frequency range of 500 Hz – 10 kHz (red solid line for the simulated data and dots for experimental data in Figure 3.5c), as opposed to less than 0.6 nm/Pa for the simulated case where the side gap space is completely filled (green dashed line in Figure 3.5c). This is more than an order of magnitude of enhancement of the mechanical sensitivity. However, it does not necessarily mean that even higher mechanical sensitivity can be achieved if a longer capillary tube is used. COMSOL TA simulation shows that for the working frequency between 500 Hz and 20 kHz, increasing the capillary tube's length beyond 2-5 mm has negligible effect on the mechanical sensitivity, as shown in Figure 3.5d for frequency at 2 kHz.

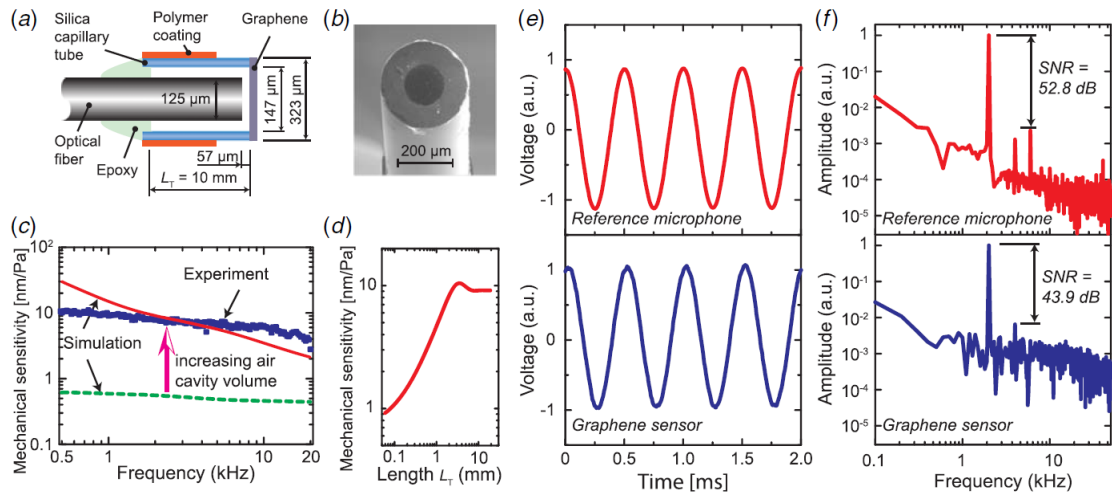


Figure 3.5 Fiber optic sensors with enlarged backing air cavity: (a) schematic of the sensor (not to scale), (b) SEM picture, (c) mechanical sensitivity spectrum: dashed line for the simulated sensitivity when there is no side gap, solid line for simulated sensitivity of the fabricated device with $L_T=10$ mm, and dots for the experiment data, (d) mechanical sensitivity at 2 kHz, simulated using COMSOL thermoviscous acoustics, as a function of the length of capillary tube L_T (denoted in (a)), (e) comparison of reference microphone and the graphene sensor in time domain at sound frequency 2 kHz, and (f) Fourier transform of the signals in (e)

At sound frequency of 2 kHz, the acquired signals from the reference measurement microphone and the graphene sensor are shown in Figure 3.5e for the time domain and in Figure 3.5f for the frequency domain. SNR of the 2 kHz signal relative to the harmonic distortion noise is 43.9 dB, which is 8.9 dB worse than the reference microphone. In comparison, the fiber optic sensor with graphene-silver diaphragm has

a SNR that is 16.8 dB worse than the reference microphone as shown in Figure 3.3e. Considering that the sensor size is merely 323 μm , smaller than the 1/2" reference microphone by a factor of 40, this miniature fiber optic sensor compares well with the much larger reference microphone.

In terms of repeatability during the test for frequencies between 500 Hz and 20 kHz, the mean value of NE is 3.05% for the fiber optic sensor and 0.63% for the reference microphone, which yields a ratio of 4.84. Although it is larger than that for the UV-molded sensor with graphene-only diaphragm (ratio of 2.27), it is largely due to the much-enhanced mechanical sensitivity, which increases by an order of magnitude.

3.5 Summary

Acoustic sensors play an important role in a variety of applications, ranging from surveillance and security, healthcare, communication, and consumer products. As graphene has been demonstrated to possess exceptional mechanical, electronic, chemical, and thermal properties, it is very natural for researchers to explore and investigate the use of graphene in developing new acoustic sensors. As sensors for measuring air-borne acoustics cannot operate without air, we have to take into account the interaction between the suspended graphene film and its backing air cavity, particularly for miniature (submillimeter) acoustic sensors to work in the audible range. Here in this thrust we have shown that mechanical sensitivity, which relates the sound stimulus to the mechanical displacement, is severely limited by the small air cavity.

This, coupled with graphene's poor reflectivity, may make one question the appeal of graphene-based optical acoustic sensors.

To address the abovementioned limitations, we investigate two approaches of developing graphene-based fiber optic acoustic sensors, each of which targets different transduction stages, given that the sensor's ultimate sensitivity S_T is the product of mechanical sensitivity S_M and optical sensitivity S_O i.e., $S_T = S_M S_O$. In the first approach (Type I), targeting the transduction stage from mechanical displacement to electronic output (i.e., S_O), a thin layer (5 nm) of silver is added on top of the graphene film before it is transferred onto a UV-molded cavity, with the aim of enhancing the sensitivity of the optical detection system. This thin layer of reflective metal layer has been experimentally demonstrated to enhance the sensitivity by three-fold. In the second approach (Type II), targeting the transduction stage from the acoustic pressure stimulus to the mechanical displacement (i.e., S_M), an enlarged backing air volume is created via the side gap between the optical fiber and the capillary tube. In this case, the distance between the fiber tip and the suspended diaphragm is kept around 60 μm to ensure a) the optical sensitivity of the sensing FP interferometer is not affected, and b) the working conditions of LCFOI system are satisfied (the cavity length of the sensing FP interferometer needs to match that of the reference FP interferometer). Experimental results show an increase of mechanical sensitivity by an order of magnitude and much improved SNR.

It is expected that the combination of the aforementioned two approaches will yield high-performance fiber optic sensors with enhanced both mechanical and optical sensitivities, based on the multiplicative relationship in $S_T = S_M S_O$. It could potentially rival the performance of the current state-of-art measurement microphones but with a much smaller footprint. For example, if the graphene diaphragm in the second approach is replaced by the graphene-silver diaphragm in the first approach, the sensor sensitivity is expected to be further enhanced.

It should also be pointed out that in the FEM simulation of small transducers, modeling becomes more challenging as the domain size becomes comparable to the thermal/viscous boundary layer thickness. The simplified analytical model based on lossless wave equation are useful to provide a general guideline. However, more accurate results need to be obtained from FEM simulation based on the Navier-Stokes equation, e.g., as implemented in COMSOL Thermoviscous acoustics.

Research outcome:

Qian Dong et al., Miniature fiber optic acoustic pressure sensors with air-backed graphene diaphragms, *Journal of Vibration and Acoustics*, 141: 041003, 2019

CHAPTER 4: DIRECTIONAL ACOUSTIC SENSORS INSPIRED BY INTERNALLY COUPLED EARS

4.1 Introduction

Acoustic sensors have been used in a wide range of applications such as surveillance and reconnaissance in military or industrial settings (J. C. Chen, Yao, and Hudson 2002; D. Li et al. 2002), hearing aids devices (Dillon 2012; Popelka et al. 2016), acoustic communication and navigation (Xiao 2010; Akyildiz, Pompili, and Melodia 2005; 2004), and structural health monitoring (Koabaz et al. 2012; Kundu 2014). In the current trend toward miniaturization, smaller, portable, and quality acoustic transducers are preferred. However, there is a fundamental size constraint to overcome in developing small acoustic sensors for sound source localization, where the most popular method to determine the sound source direction is based on the time difference of arrival (TDOA) (Benesty, Chen, and Huang 2008; Brandstein and Ward 2013). For a microphone pair $TDOA = d\sin(\theta)/c_0$, where d is the separation and c_0 is the sound speed. As TDOA is linearly proportional to d , there is a fundamental size limit in sound source localization: the smaller the separation, the worse the performance. In other words, the signals received by two closely placed microphones are essentially indistinguishable. As such, the microphones need to be separated greater than a critical distance, depending on factors such as signal-to-noise ratio, choice of estimator, and number of samples.

To address this fundamental size limit, a solution needs to be sought to overcome the size constraint, for which we may seek inspiration from the Nature. Internally coupled ears (ICE) (van Hemmen et al. 2016) (a.k.a. pressure difference receivers (Axel Michelsen and Larsen 2008)) exist in more than half of the terrestrial vertebrates (e.g., frogs (Narins 2016; Bee and Christensen-Dalsgaard 2016), lizards (J. Christensen-Dalsgaard 2005; Carr, Christensen-Dalsgaard, and Bierman 2016; Jakob Christensen-Dalsgaard and Manley 2008), birds (Kettler et al. 2016; Larsen, Christensen-Dalsgaard, and Jensen 2016), and crocodylians (H. S. Bierman et al. 2014; Hilary S. Bierman and Carr 2015; Carr, Christensen-Dalsgaard, and Bierman 2016)) and many insects (e.g., grasshoppers (Axel Michelsen and Rohrseitz 1995; Römer and Schmidt 2016), crickets (Schmidt and Römer 2013), and cicadas (Fonseca and Hennig 2004)). ICE can take a variety of forms, mostly involving two tympanic membranes (eardrums) and an air-filled interaural cavity, which may consist of several interconnected air sacs. Lizards have been demonstrated to have the strongest internal coupling (Jakob Christensen-Dalsgaard 2011; 1985; J. Christensen-Dalsgaard 2005; Jakob Christensen-Dalsgaard and Manley 2008; Carr, Christensen-Dalsgaard, and Bierman 2016). In their best frequencies of hearing at 1-3 kHz, the sound wavelength (11-34 cm) is much larger than its head size (~1 cm). Hence, interaural level difference (ILD) due to diffraction is minimal. However, the eardrum of the lizards exhibits strong directionality, with maximal directionality up to 40 dB; interaural phase difference (IPD) or the equivalent interaural time difference (ITD) exhibited by the eardrums is three times or larger than that at the input (Jakob Christensen-Dalsgaard and Manley 2008).

Inspired by the working principle behind ICE, Miles connected two commercially available Knowles directional microphones for hearing aids (Miles 2016). He concluded a dramatic improvement of sensitivity and noise floor, when compared with the difference of signals from two omni-directional microphones. Targeting sound source localization, in this Thrust, a holistically designed acoustic sensors is presented with two diaphragms coupled by a connecting cavity with the aim of achieving large amplification of directional cues IPD/ITD.

4.1.1 Directional Hearing in Animals

To detect the direction of a sound source, the directional hearing of animals usually rely on two acoustic cues such as interaural time difference (ITD) and interaural level difference (ILD). In mammals, the separation distance between two eardrums is at least 50 mm, which means the time difference is greater than 145 μ s. Mammals are able to take advantage of its complex peripheral structures and measure ILD. In addition, when the dimension of the head is larger than one-tenth of the sound wavelength, the sound wave will be disturbed (diffracted). In this case, human brain can further differentiate the spectra difference between the two ears. In the case of a narrow-band sound source, the spectra difference reduces to the IID at the center frequency. Human ears can also localize long pure tones that are less than 1400 Hz by extracting the time difference of arrival (TODA, equivalent to ITD) at the two ears. Given that the head diameter is about 17 cm and sound speed in air is 344 m/s, this time difference can be as large as 0.5 ms.

However, for small species, narrow-band sound is commonly utilized given their limited capacities of signal processing. Because the part of the body that the ears are placed is about 10 to 50 times smaller than the human's head, the diffraction occurs only at high frequency range, and the expected maximum ITD is in the ranges of tens of microseconds or even smaller. For the small reptiles, the body length is only from 0.1 cm to 40 cm and the separation between the auditory organs is about 20 mm. The corresponding ITD is 58 μ s, and ILD is normally smaller than 4 dB. Thus, how the small species can localize sound source despite their limited auditory system has attracted a lot of interest from researchers.

4.1.2 Internally Coupled Ears (ICE)

ICE is found in the hearing system of small terrestrial vertebrates, in which the two tympanic eardrums are interconnected by an air-filled passageway that exist within skull or oral space. Although a binaural connection is also found in human, which is called as Eustachian tube, this connection is too narrow to allow sound propagation. However, the connection of ICE animals is large enough for the transmission of sound wave, as evidenced by cochlear microphonic measurement (Rosowski and Saunders 1980). The two eardrums in ICE are not only driven by an external pressure from the sound source but also an internal pressure transmitted from the opposite eardrum. Due to this net-pressure, the ICE can significantly amplify the time differences. In other words, this middle ear structure is the reason why small terrestrial animals can still localize the sound when their binaural distance is at least ten times smaller than the

wavelength of their interested frequency. It is important to note here that not all the birds have this ICE structures, such as barn owls, it only has an isolated middle ear, and its interested frequency range is higher enough to generate sufficiently large ILD (Coles and Guppy 1988). For small animals with ICE, the diffraction of the sound wave by its head is negligible and the pressure intensity impinging on the two eardrums is similar. Hence, the internal loading on the eardrums plays a critical role in determining the directionality. The key is how the intensity and phase of the sound wave changes as it propagates through the passageway. The heads of most lizard heads are 10-20 mm in diameter, much smaller than the wavelength in their interested frequency range from 1 kHz to 4 kHz (85-340 mm in wavelength). However, Christensen compared the directional hearing ability of four different types of lizards including *M.macularia*, *L.bellinan*, *C.similis*, and *G.gecko* (J. Christensen-Dalsgaard 2005). He demonstrated that the lizard's ears are highly directional in an extensive frequency range with ILD up to 40 dB.

4.1.3 Lumped Model for Air-born Coupling ear

To explain the high directional hearing in animals with ICE, Fletcher came up with a general circuit lumped model (Fletcher 1992). As shown by Figure 4.1a, two eardrums and one cavity are modeled as two impedance elements (Z_T or Z_V). The governing equations for the two loops are given by:

$$Z_T U_1 + Z_V (U_1 + U_2) = P_1, \quad Z_T U_2 + Z_V (U_2 + U_1) = P_2, \quad (6)$$

where p_1 and p_2 are the pressure applied to the external side of eardrums from a plane wave, U_1 and U_2 are the volum flows in the two loops. Neglecting diffraction, the two pressures have same amplitudes but differ in phase by

$$\Delta\varphi = \left(\frac{\omega}{c}\right) d\sin\theta, \quad (7)$$

where ω is the angular frequency, c is the sound speed, d is the interaural distance, and θ is the sound incidence angle relative the normal direction. $U_{1,2}$ can be calculated by:

$$U_1 = \frac{p_1(Z_T+Z_V)-p_2Z_V}{Z_T(Z_T+2Z_V)}, \quad U_2 = \frac{p_2(Z_T+Z_V)-p_1Z_V}{Z_T(Z_T+2Z_V)} \quad (8)$$

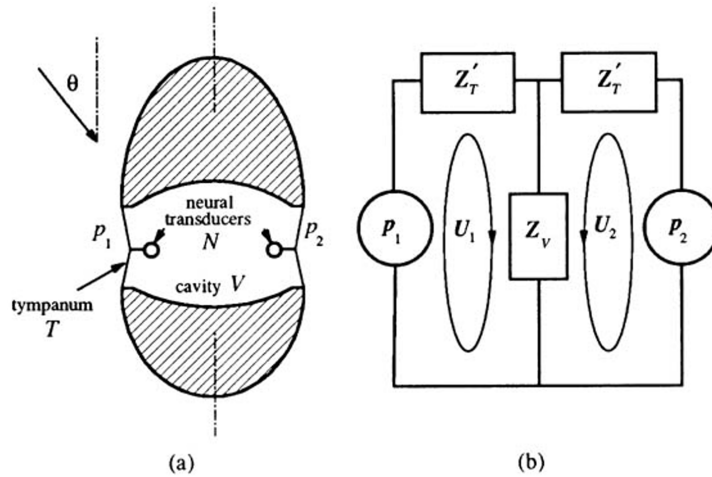


Figure 4.1. Existing ICE model. (a) An auditory system consisting of two simple ears coupled acoustically through a closed cavity. (b) The corresponding lumped model.

4.1.4 Transmission Gain (TG) Calculation

Due to the critical role of coupling strength for directionality, Michelsen et al. presents an experimental method to measure the coupling strength, characterized by a terms knowns as transmission gain (TG) (A. Michelsen et al. 1994). A local stimulation experiment is used for TG measurement, as shown in Figure 4.2. Two eardrums are acoustically isolated by a wall of wax. In other words, only one eardrum is exposed to the acoustic stimulus from the speaker.

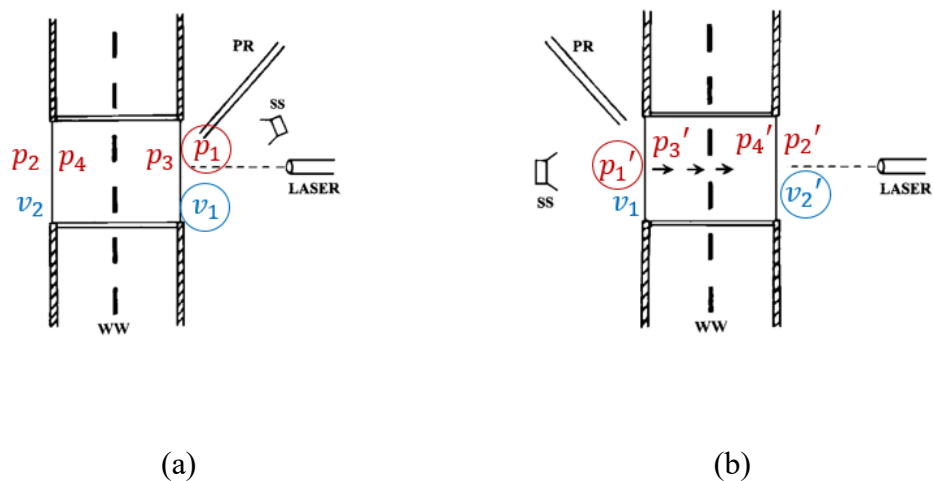


Figure 4.2. Local stimulation for transmission gain measurement. (a) Step 1: measure pressure P_1 and velocity v_1 of ipsilateral eardrum. (b) Step 2: to measure the closed field pressure P_1' at ipsilateral side and normal velocity v_2' of contralateral eardrum.

In this method, TG can be directly found from two transfer functions with two steps measurement. In the first step, as shown in Figure 7(a), a laser Doppler vibrometer

(LDV) is used to measure the center velocity of the ipsilateral eardrum (v_1), and its external pressure (P_1) can be obtained by a pressure probe. Due to the isolation by a wall of wax, the contralateral eardrum has no external pressure stimulus ($P_2 = 0$). Therefore, it is only excited by its internal pressure (P_4). In the second step, as shown Figure 7(b), both the speaker and pressure sensor are moved to the other side, and the ipsilateral pressure (P_1') and the velocity v_2' of contralateral eardrum are obtained.

Based on these two measurements and assuming the organs are symmetric, the transfer functions for the eardrums can be written as:

$$\frac{v_1}{P_1 - P_3} = \frac{v_1'}{P_2' - P_4'} \quad (9)$$

where P_3 is negligible because it is much smaller than the external pressure in the first step, and P_2' is equal to zero due to the sound isolation. Defined as the coupling strength between the two eardrums, TG can be calculated as P_4/P_1 or v_2/v_1 .

4.2 Design of Bio-inspired Pressure Different Receiver

Inspired by the working principle behind ICE, Miles connected two commercially available Knowles directional microphones for hearing aids (Miles 2016). He concluded a dramatic improvement of sensitivity and noise floor, when compared with the difference of signals from two omni-directional microphones. However, a

fundamental understanding of working mechanism of internal coupling is still lacking, and no design guidelines have been provided.

According to the Fletcher model, the impedance of the connecting cavity Z_V largely determines the coupling strength, which will be the focus of sensor design based on the parameters listed in Table 4.

Table 4.1: Physical parameters for a cavity-coupled auditory system

Separation of ears (sphere)	20 mm
Tympanum area	20 mm ²
Tympanum thickness	10 μm
Effective transducer mass	1 mg
Loaded Tympanum resonance	500 Hz
Q of loaded tympanum	1
Cavity volume	1 cm ³

COMSOL Thermoviscous Acoustics will be used here to carry out the FEM simulation for the designed sensor, as shown in Figure 4.3a for the FEM model. To reduce the simulation time, symmetric boundary condition is applied. An eigen analysis shows that there are multiple anti-symmetric and symmetric modes for this internally coupled

structure. The first two modes, denoted as the rocking and bending modes, are shown in Figure 4.3b. In rocking mode, the two diaphragms are 180° out of phase (one inward and one outward); whereas in bending mode the two diaphragms are in phase.

Next, one loading method is used to obtain the center deflections of the two diaphragms when only one eardrum is excited by a unit pressure (1 Pa), recorded as A_{ipsi} and A_{contra} where the subscripts ipsi and contra denote the diaphragm at the same side as and away from the pressure stimulus. When a plan wave with azimuth θ and unit amplitude is incident on the sensor (assuming the diffraction of the plane wave by the sensor is negligible), the center deflections and IPD can be obtained by

$$x_{ipsi} = A_{ipsi}e^{\frac{ikd \sin \theta}{2}} + A_{contra}e^{\frac{-ikd \sin \theta}{2}} \quad (10)$$

$$x_{contra} = A_{ipsi}e^{\frac{-ikd \sin \theta}{2}} + A_{contra}e^{\frac{ikd \sin \theta}{2}} \quad (11)$$

$$IPD = angle\left(\frac{x_{ipsi}}{x_{contra}}\right) \quad (12)$$

Here, k is the wavenumber and d is the interaural separation.

The simulated IPD at $\theta = 90^\circ$ is shown in Figure 4.3c as a function of frequency, where a great amplification (a factor of 6) is seen near the rocking mode when compared with the coupled case. To investigate how the volume of the connecting cavity affects the

sensor performance, a parametric study is carried out for different coupling conditions: “strong” coupling ($V = 0.1 \text{ cm}^3$), “medium” coupling ($V = 1 \text{ cm}^3$), and “soft” coupling ($V = 2 \text{ cm}^3$). As shown in Figure 4.3d, when the coupling is strong (small volume $V = 0.1 \text{ cm}^3$), maximum amplification of the IPD can be achieved. However, when θ increases from 0° to 90° , IPD quickly increases and saturates at 180° . The downside of this maximum amplification is that the directional sensitivity is poor in most of the azimuth range. On the other hand, when the coupling is soft (large volume $V = 2 \text{ cm}^3$), the amplification of IPD is not significant. When the cavity volume of lizards ($V = 1 \text{ cm}^3$) is used, the amplified IPD is a good compromise with both a high amplification ratio and a wide working azimuth angle range.

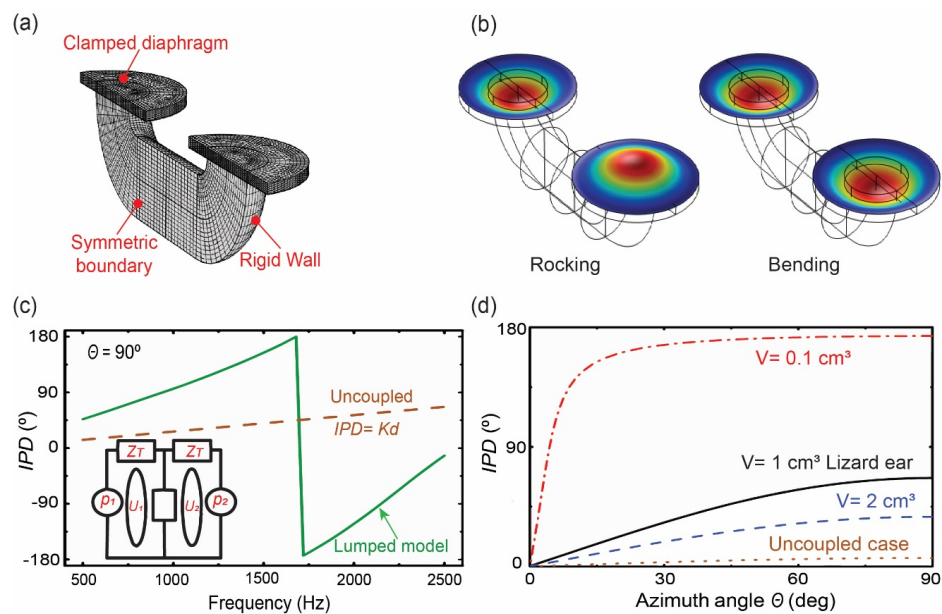


Figure 4.3. Low-frequency auditory models. (a) FEM model using COMSOL Multiphysics. (b) The first two mode shapes: the rocking mode (left) and the bending

mode (right), (c) IPD at azimuth 90° as a function of frequency based on the Fletcher model, which is shown in the inset. (d) IPD at 1 kHz as a function of azimuth when the volume of the connecting cavity is varied.

4.3 Sensor Fabrication and Integration

Based on the insights gained from the FEM simulation, a large-scale bio-inspired sensor is design. As shown in the top of Figure 4.4a, the sensor consists of two clamped circular diaphragms connected by a U-shaped air channel. The substrate is 3D-printed using polyactic acid (PLA). There are two through holes from the backside to facilitate the insertion of ceramic ferrules which serves as guides for optical fibers. To detect the vibrations of each of the two diaphragms, a low-coherence fiber optic interferometric (LCFOI) system is employed, as shown in the bottom of Figure 4.4a. In this system, a superluminescent light emitting diode (SLD) is used as the light source, two tunable Fabry-Perot filters as reference interferometers, and the cavity between the fiber end and diaphragms as a Fabry-Perot sensing interferometer. The output of each photodetector measures the difference between the reference interferometer and the sensing interferometer. The diaphragms are made of commercial aluminum foil with 8 mm for the radius and $17.78 \mu\text{m}$ (or 0.7 mil) for the thickness. The binaural separation of 25.4 mm is chosen based on the average head size of lizards. Before the two diaphragms are glued to the washers, they are heated to 70°C above the room temperature. When they are cooled back to the room temperature, in-plane tension is generated in the diaphragms.

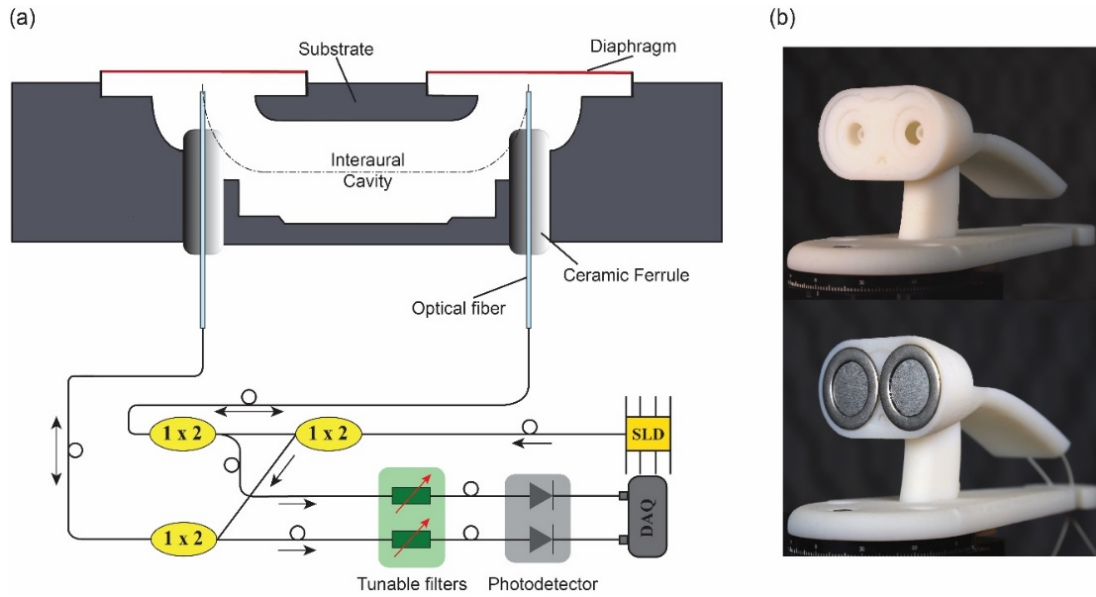


Figure 4.4: Bio-inspired directional acoustic sensor. (a) Schematic of sensor (top) and a low-coherence fiber-optic interferometric system (bottom). (b) Photo of the sensor before (top) and after (bottom) attaching the diaphragm.

4.4 Sensor Characterization

To characterize the fabricated device, a swept pure tone is used to stimulate the sensor mounted on a motorized stage. IPD is obtained as a function of sound frequency and azimuth, as shown in Figure 4.5a for the surface plots comparing the experimental and simulation results, which has a good agreement. Notice that IPD has a sign change around 1.7 kHz, the natural frequency for the rocking mode. This finding can be confirmed by plotting IPD at $\theta = 90^\circ$ as a function of frequency. See Figure 4.5b, where the inset shows the mode shape of the rocking mode. For the sake of comparison, an un-coupled device is printed and fabricated with the same procedure except that the

internal cavity is blocked. Clearly, the internal coupling enables the great amplification of phase difference.

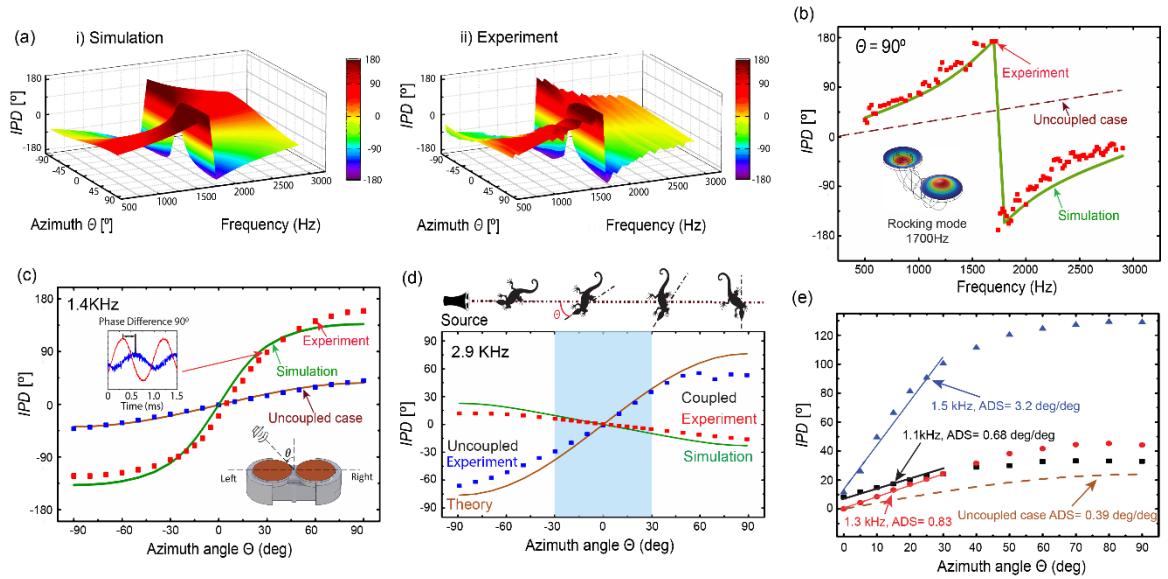


Figure 4.5. Characterization of the prototype. (a) Surface plot of IPD comparing the simulation (i) and experimental results (ii). (b) IPD at 90° incident as a function of frequency (inset shows the mode shape for the rocking mode). (c) IPD versus azimuth angles at frequency 1.4 kHz. (d) IPD versus azimuth angles at frequency 2.9 kHz. (e) Calculation of the average directional sensitivity (*ADS*).

Working at 1.4 kHz, IPD is plotted as a function of azimuth in Figure 4.5c. Comparing the uncoupled and coupled cases shows that the internal coupling amplified the phase difference by a factor of 5. On the other hand when working at 2.9 kHz (Figure 4.5d), the phase difference is not amplified at all as the frequency is close to the bending mode.

Note that localization performance depends not only on the value of phase difference but even more importantly, on the variation of IPD with respect to the azimuth. For this purpose, average directional sensitivity(ADS) is calculated from the linear range of IPD curves which is between -30° and 30° , as illustrated in Figure 4.5d. For three frequencies 1.1 kHz, 1.3 kHz, and 1.5 kHz, ADS increases from 0.68 deg/deg at 1.1 kHz to 3.2 deg/deg at 1.5 kHz.

4.5 Summary

An inherently directional acoustic sensor mimicking the internally coupled ears found in many animals is investigated in this Thrust. The sensor consists of two individual diaphragms coupled by an air-filled U-shaped channel. A prototype has been fabricated and characterized, which shows a great amplification of interaural phase difference ($\sim 6.6x$) at 90° and a directional sensitivity ($\times 10$) for a wide frequency range. In terms of the equivalent phase difference or directional sensitivity, it is equivalent to a conventional microphone pair that is separated further apart by an order of magnitude. Extending this proof-of-concept sensor to MEMS size devices will enable the development of miniature directional sensors for a variety of applications requiring small sensors but high directional sensitivity.

Research outcome

Qian Dong and Haijun Liu, An optical acoustic sensor for sound source localization inspired by internally coupled ears, *Journal of the Acoustical Society of America Express Letter*, in submission.

CHAPTER 5: ACOUSTIC METAMATERIALS WITH AIR-COUPLED DIAPHRAGMS

5.1 Introduction

Metamaterials are frequently defined as artificial materials engineered to realize properties that have not been found in nature (Kshetrimayum 2004). Consisting of repeating patterns (a.k.a. unit cells) at scales much smaller than the wavelength of interest, metamaterials provide a new way to manipulate waves through controlling the configuration (size, shape, orientations, etc.) of the unit cells. Similar to its optical counterpart (Shelby, Smith, and Schultz 2001; D. R. Smith and Kroll 2000), acoustic metamaterials (AMM) are designed to manipulate sound waves by tailoring its effective mass density and bulk modulus of the unit cells (J. Li and Chan 2004; Yao, Zhou, and Hu 2010). In recent years, the concept of AMM has been extended beyond the scope of negative refraction materials and found in applications such as acoustic super-resolution, acoustic cloaking based on transformation acoustics, zero-index medium, acoustic meta-surface, and nonreciprocal acoustic devices (F. Ma et al. 2015).

Among the various types of AMM, a number of membrane-based AMM have been reported to take advantage of its lightweight, simple geometry and the ability to tune the effective density (Huang, Shen, and Jing 2016). A typical configuration of the unit cell consists of a clamped membrane (or plate) with or without a mass attached to the center. At the resonant frequencies, the membrane has a large displacement/velocity in response to acoustic excitation, which is associated with high transmission. At the anti-

resonance frequencies, the membrane has minimum displacement/velocity, acting effectively as rigid reflectors. In terms of the effective density, it is negative below the first resonance frequency.

Applied to acoustic absorption, membrane-based AMM has been demonstrated to obtain almost 100% acoustic absorption at low frequencies (G. Ma et al. 2014). For sound in the audible frequency range of 20 Hz to 20 kHz, the viscous dissipation in the vicinity of solid surfaces, such as plastic foam, glass fiber, and mineral wool, is the conventional method to dissipate the acoustic energy. Since the dissipative force varies linearly as a function of the flux rate, dissipated power (the product of force and flux) is a quadratic function of frequency (Szabo 1994). Hence, there is a fundamental limitation to achieve high acoustic absorption for low frequency. To this end, AMM provides an alternative approach based on local resonances, where sub-wavelength unit cells can be designed to have resonance frequency in low frequency and be configured to form a large thin panel, potentially addressing the fundamental limit of sound attenuation and absorption.

In a representative example, Sheng and his group demonstrated a membrane-based AMM based on hybrid resonances (G. Ma et al. 2014). The unit cell consists of a diaphragm decorated by a rigid center mass and clamped to a rigid substrate, a backing gas cavity filled with SF₆, and a rigid aluminum back plate. The presence of the backing gas changes the vibration modes of the membrane (i.e., hybridization). When the membrane tension and depth of the sealed gas cavity are tuned properly, the impedance

of the membrane is perfectly matched with air, thus absorbing all the incident energy. Perfect absorption was demonstrated simultaneously at three different frequencies (255, 309, and 420Hz) with three-unit cells, each having different center masses (0.18 g, 0.12 g, and 0.06 g) and different gas cavity depths (30 mm, 25 mm, and 15 mm).

However, the absorption bandwidth in most reported AMM is very narrow around some local resonance frequency (e.g., $< \sim 5$ Hz in (G. Ma et al. 2014)), which limits its practical use. This thrust seeks to achieve a fundamental understanding of broadband acoustic absorption using AMM and presents some preliminary numerical and experimental results. In the rest of the sections, we will first establish a theoretical framework for unit cells of air-backed diaphragms based on the impedance matching principle. Here, the term of the diaphragm is used as it encompasses pure membrane, pure plate, or cases in between (Sheng et al. 2003). The goal is to understand the conditions for achieving large absorption bandwidth. Then, three different approaches will be numerically studied, followed by preliminary experimental results.

5.2 Theoretical Framework Using Impedance Matching

The focus of this thrust is on AMM thin panels with a periodic arrangement of unit cells (Figure 5.1a) to achieve broadband and high acoustic absorption. As shown in Figure 5.1c-d for the unit cell, the main component is a circular diaphragm (diameter d and thickness h_d) clamped to a rigid frame and backed by a cylindrical air cavity (length h_c). Based on our previous study on the acoustic-structural interaction (Liu, Olson, and

Yu 2014b), the combined air-diaphragm system can be modeled as an equivalent mass-spring-dashpot ($m'-s'-R_m'$) system, as illustrated in Figure 5.1d. The corresponding mechanical impedance is $Z'_m = R'_m + j(m'\omega - s'/\omega)$. Assuming the incident plane wave is $p_{in} = P_{in} \exp(j\omega t)$ and the reflected wave is $p_r = P_r \exp(j\omega t)$ the reflection coefficient can be obtained as

$$R = \frac{p_r}{p_{in}} = \frac{Z'_m A - Z_a}{Z'_m A + Z_a} = \frac{R'_m A - \rho_0 c_0 + jA(m'\omega - s'/\omega)}{R'_m A + \rho_0 c_0 + jA(m'\omega - s'/\omega)} \quad (13)$$

where A is the effective area of the mass, ρ_0 and c_0 are the density and speed of sound of air, respectively. Therefore, the acoustic absorption can be obtained as follows:

$$\alpha = 1 - |R|^2 \quad (14)$$

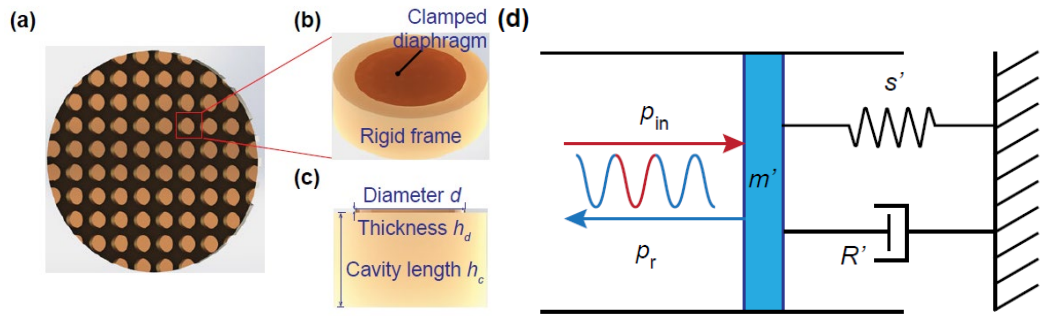


Figure 5.1: Acoustic metamaterial thin panel for broadband acoustic absorption. Schematic of the panel (a) and unit cell (b), whose dimensions are shown in (c) and lumped model in (d).

In order to achieve 100% absorption (i.e., 0% reflection), it can be seen from Eq. ($R = \frac{p_r}{p_{in}} = \frac{Z'_m A - Z_a}{Z'_m A + Z_a} = \frac{R'_m A - \rho_0 c_0 + jA(m'\omega - s'/\omega)}{R'_m A + \rho_0 c_0 + jA(m'\omega - s'/\omega)}$) that two conditions need to be satisfied (both the real and imaginary parts of the numerator need to vanish): $R_m = \rho_0 c_0$ and $m\omega - s/\omega = 0$, i.e., the impedance of the lumped system matches with that of the air at its resonant frequency $\omega_n = \sqrt{s/m}$. Defining the impedance matching factor as $\beta = R_m / (\rho_0 c_0)$, we can obtain the absorption spectra for different values of β , as shown in Figure 5.2a using the parameters listed in Table 5 for a fixed resonant frequency $\omega_n = 1$ kHz. It can be clearly seen that 100% absorption is only achievable when $\beta = 1$, which can also be verified from Figure 5.2b where the peak absorption is plotted as a function of β using the analytical formula $\alpha_{\text{peak}} = 4\beta / (\beta + 1)^2$.

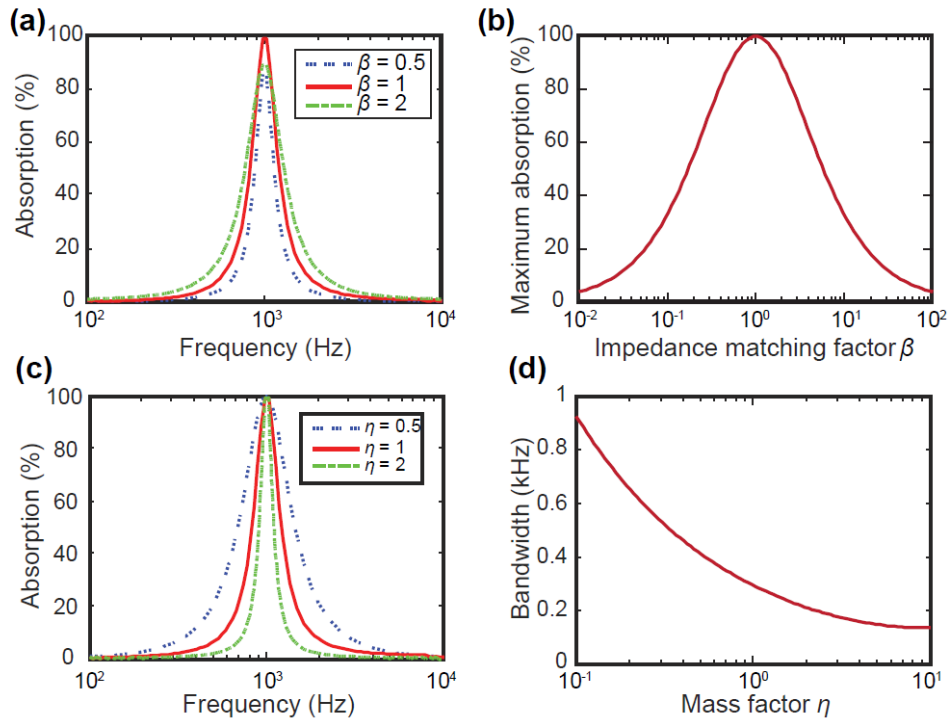


Figure 5.2 Absorption properties of AMM obtained from the analytical lumped model.

(a) Absorption spectra for three different values of impedance matching factor β ($\beta = 1$ for the matched impedance case). (b) Maximum absorption as a function of β . (c) Absorption spectra for three different values of mass factor η when $\beta = 1$ (the bigger the value of η , the heavier the effective mass). (d) Absorption bandwidth as a function of η .

In terms of the bandwidth (full width at half maximum), it can be derived as $\Delta\omega = (\beta + 1)\rho_0 c_0 / m$. As seen in Figure 5.2a, the bandwidth increases when the effective damping increases. More importantly, the bandwidth is inversely proportional to the effective mass. Defining the mass factor η as the ratio of the equivalent mass relative

to the nominal value given in Table 5, the absorption spectra for different values of η are studied while keeping the resonant frequency at 1 kHz. It can clearly be seen from Figure 5.2c-d that increasing the effective mass will lead to smaller bandwidth. From these results based on the simple lumped model, we can see that the key to obtain a broad absorption bandwidth around a local resonant frequency is to have lighter diaphragm, which is different from most reported membrane-based AMM, typically with a relatively heavy center mass. Based on these insights, we will investigate using a single uniform diaphragm to ensure large absorption bandwidth. The focus will then be on how to satisfy the impedance matching condition tuning the effective damping R_m .

Table 5.1: Parameters for the analytical lumped model

Density of air (ρ)	1.24 kg/m ³
Sound speed (c_0)	343 m/s
Cross-section area (A)	707 mm ²
Effective mass (m')	0.25 g
Effective spring constant (s')	9,923 N/m
Resonance frequency (ω_n)	1000 Hz

5.3 AMM Design Using Numerical Simulation

Based on the analysis in the previous section, the effective damping coefficient R'_m needs to be equal to $\rho_0 c_0 A$ so that the real part of the diaphragm's impedance matches with that of air. The question is how to tune the damping, given that the intrinsic damping of the diaphragm is typically small and constant. We previously studied the acoustic-structural interaction between the diaphragm and the backing cavity and found that the backing cavity changes the effective mass, stiffness, and damping of the diaphragm (Liu, Olson, and Yu 2014b). In this section, we will investigate three approaches to tune the effective damping, including the length of backing air cavity h_c , the static pressure of the air cavity p_0 , and the thickness of the perforated plate h_p .

To take into account the viscous loss in the air cavity, a finite element method (FEM) model is developed using the Thermoviscous Acoustic (TA) module in COMSOL 5.3a, which is based on the linearized Navier-Stokes equations. Taking advantage of the symmetry, as shown in the FEM model in Figure 5.3a, only a 30° segment is modeled: the air cavity is meshed using second-order brick elements, the diaphragm is meshed using quadrilateral shell elements, and boundary layer meshes are added near all the rigid walls. The diaphragm is made of polyimide film (DuPont Kapton) with a thickness of 1 mil (i.e., 25.4 μm) and diameter of 16.6 mm. A constant Rayleigh damping coefficient $\alpha_0=500$ 1/s is used based on our previous experimental results. To excite the diaphragm, a dynamic pressure loading with unit amplitude ($p = e^{i\omega t}$ Pa) is uniformly applied to the outer surface of the diaphragm. The mechanical impedance is

calculated by $Z_m = p/v$, where v is the average surface velocity of the diaphragm. Thus, the impedance matching factor can be obtained as $\beta = \text{Re}(Z_m)/(\rho_0 c_0)$. As for controlling the in-plane tension, the diaphragm will be heated in an oven to a higher temperature T while it is glued to a stainless washer. When it is taken out of the oven and cools down to the room temperature T_0 , a uniform tension is generated that is linearly proportional to the shrinkage temperature $\Delta T = T - T_0$. Figure 5.3b shows the effect of the backing air cavity in changing the mode shape, i.e., hybridization.

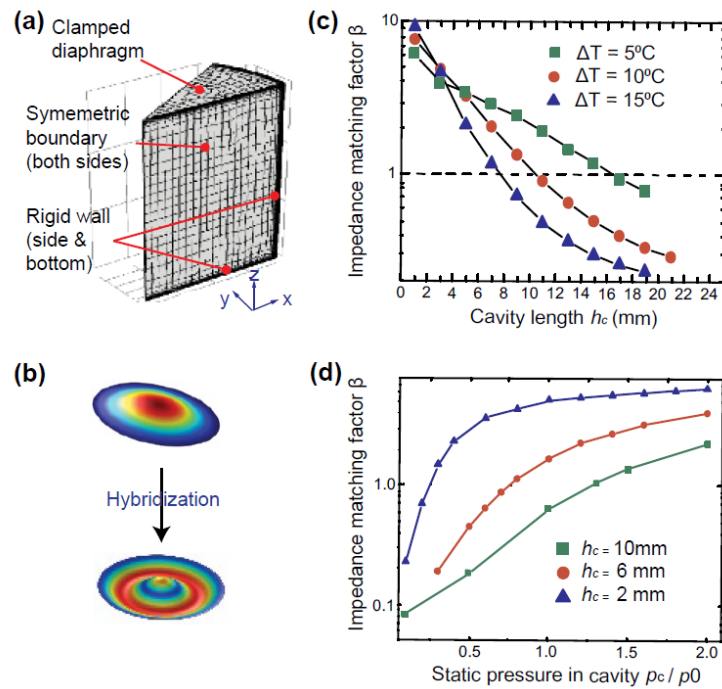


Figure 5.3: Tuning the effective damping using a straight cylindrical air cavity. (a) FEM model in COMSOL. (b) Mode shape of the fundamental mode before (top) and after (bottom) hybridization. (c) Impedance matching factor β as a function of cavity length

h_c for three difference shrinkage temperatures ΔT . (d) β as a function of the static pressure in the cavity for three different h_c values.

In the first approach, the cavity length h_c will be tuned. Figure 5.3c shows the impedance matching factor β as a function of h_c for three different values of ΔT (5°C, 10°C, and 15°C). It can be observed that β increases as the cavity becomes shorter. This can be explained by the value of h_c relative to the boundary layer thickness h_b (69.3 μm thick at 1 kHz). As h_c shrinks and starts to be comparable to h_b , the viscous effects become more pronounced. For diaphragm with larger in-plane tension (larger ΔT such as 15°C), the diaphragm is stiffer and therefore requires a shorter h_c to reach the impedance matching condition ($\beta=1$). For example, the critical value of h_c to ensure $\beta=1$ is ~ 8 mm for $\Delta T = 15^\circ\text{C}$, but 17 mm for $\Delta T = 5^\circ\text{C}$. Note when the cavity is in the short region ($h_c \ll 4$ mm), the stiffness contributed by the air cavity dominates that of the diaphragm itself. As such, the effective damping coefficient is less sensitive to the in-plane tension. That is why the three curves in Figure 5.3c almost overlap on each other in this short region.

In the second approach, the static pressure in the backing air cavity p_b is another parameter that can be theoretically used to tune the damping. Figure 5.3d shows the impedance matching factor as a function of p_b normalized by the ambient pressure p_0 for three values of h_c (10 mm, 6 mm, and 2 mm) and same ΔT (10°C). In all three cases,

as the air particles become denser (larger value of p_b), the viscous effect increases, which leads to larger effective damping for the diaphragm.

Different from the above two methods, a third approach adds a perforated back plate in the air cavity, serving similar functionalities in condenser microphones for tuning the effective damping. As shown in the inset of Figure 5.4, a perforated plate with an array of small holes (1 mm for the diameter and 2 mm for the spacing) is added in the middle of the air cavity. Again, TA module in COMSOL is used to simulate the thermoviscous loss at the boundary of small holes. Figure 5.4 plots the impedance matching factor β as a function of the thickness of the perforated plate h_p . The simulation results show that the effective damping increases as the perforated plate becomes thicker.

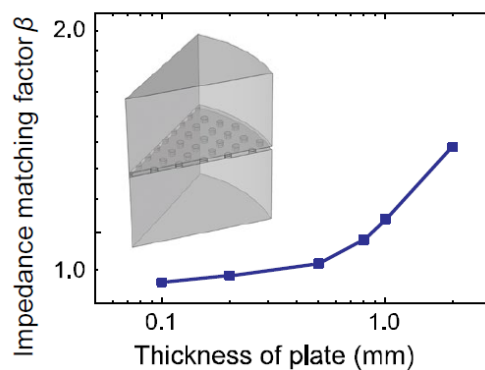


Figure 5.4: Tuning the effective damping by adding a perforated plate and changing its thickness. Inset shows the schematic in COMSOL.

Among the studied three approaches, the first approach is the simplest and most practical. As such, a preliminary experimental study is conducted to verify the feasibility.

5.4 Experimental Results

The experimental measurement is based on an impedance tube (Brüel & Kjær 4206-T), as shown in Figure 5.5a. It features a loudspeaker at one end and four microphones positioned on the sidewall (two upstream and two downstream). The test sample is fixed in the middle and an anechoic termination is used to seal the tube end. Instead of using broadband white noise excitation, the approach described in ref. (Ho et al. 2005) is implemented to use swept sine to ensure better signal-to-noise ratio and more accurate measurements.

5.4.1 Tuning by Varying Cavity Length

Based on the simulation results to ensure matched impedance, the cavity length is determined to be 17 mm for shrinkage temperature of $\Delta T = 5^\circ\text{C}$. To fabricate the unit cell prototype, first, the substrate is 3D printed using polyacrylic (PLA) filaments. Then, a circular 2-mil polyimide film is heated to 5°C above the room temperature in an oven while being glued to a steel shim. When it cools down to the room temperature, a uniform initial tension is generated in the film. Lastly, the steel shim is pressed into a groove in the 3D printed substrate. The back end of the plastic substrate can be considered rigid. See the inset of Figure 5.5b for a photo of the prototype.

The measured absorption spectrum is plotted in Figure 5.5b. The peak absorption is found to be 98% at the resonance frequency of 1.45 kHz. More importantly, the bandwidth (FWHM) is found to be 200 Hz, significantly larger than that of AMM with heavy center mass, verifying the feasibility of our approach. The corresponding quality factor can be calculated as $Q = \sim 7$. To further increase the bandwidth, multiple unit cells can be combined in a single AMM panel, as long as the spacing is much smaller than the wavelength of interest.

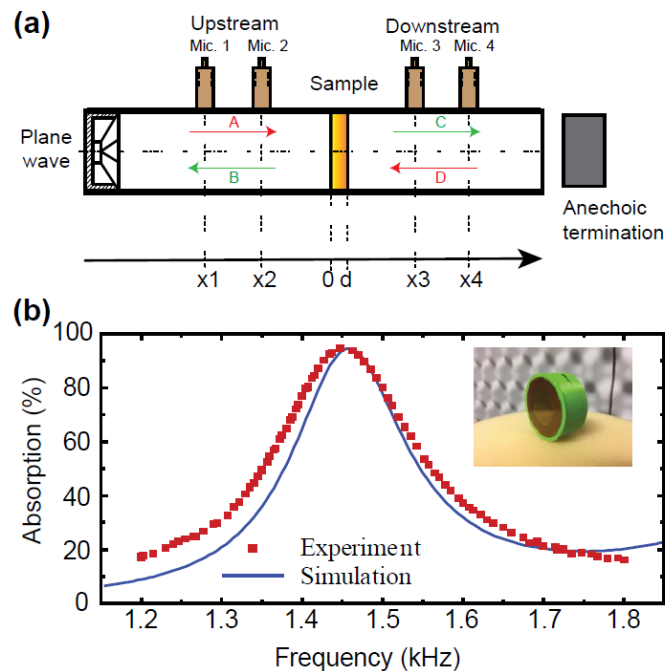


Figure 5.5: Preliminary experimental results. (a) Experimental setup based on an impedance tube (B&K Type 4206). (b) Absorption spectrum for a prototype with 17 mm length cavity.

5.4.2 Tuning by Using Micro-Perforated Plates (MPP)

MPP has been widely studied as a micromechanical structure (Homentcovschi and Miles 2005; Bao et al. 2003) that is featured with densely punched holes on a rigid plate. These hard plates, usually, are hard enough to be a rigid reflector for airborne waves. In other words, the functional part of MPP for absorption are those punched holes that have diameters of ~ 1 mm, so-called micro-perforation. Based on the insights from previous simulation results, a 3D printed MPP (red), as shown in Figure 5.6a, was inserted into the middle of the cylindrical cavity for further tuning the equivalent damping. The absorption spectra for punched holes with two different diameters (1 mm and 2 mm) are plotted in Figure 5.6b, along with the case without adding MPP. A longer cavity length, 40 mm, was chosen to provide a smaller damping ($\beta < 1$). A 2-mil polyimide diaphragm with a pre-tension from 5°C thermal expansion was used. Two MPP samples are 3D printed with same thickness ($W = 2$ mm) and same area density ($\sigma = 40\%$), but different diameters (1 mm and 2 mm). As shown in Figure 5.6b, the damping factor increases as the diameter decreases and approaches the matched impedance ($\beta = 1$). As a result, the maximum absorption increases from 90-95% to nearly 100%. The absorption bandwidth (FWHM) increases with enhanced damping when smaller perforated holes are used. A resonance shifting was observed when MPP was added: 1.11 kHz for the sample without MPP, 1.12 kHz for the $\varnothing - 2$ mm MPP, and 1.13 kHz for the $\varnothing - 1$ mm MPP. This shift can be explained by the change of the effective stiffness of the backing cavity. As the diameter perforated holes decrease, the volume of the backing air cavity decreases, leading to the increased stiffness. In

addition to enhancing the viscous dissipation through the perforate holes, MPP also changes the effective inertia. The effective mass can be derived as $m'' = M/\sigma = \rho(\pi a^2 W + \frac{4\pi}{3} a^3)/\sigma$ (Moser 2014), which is the sum of the mass in the cylindrical hole ($\rho\pi a^2 W$) and the mass of a sphere ($\rho \frac{4\pi}{3} a^3$). As discussed in Chapter 2 and Chapter 3, the inertial effect becomes important when it is in the mass-dominated region.

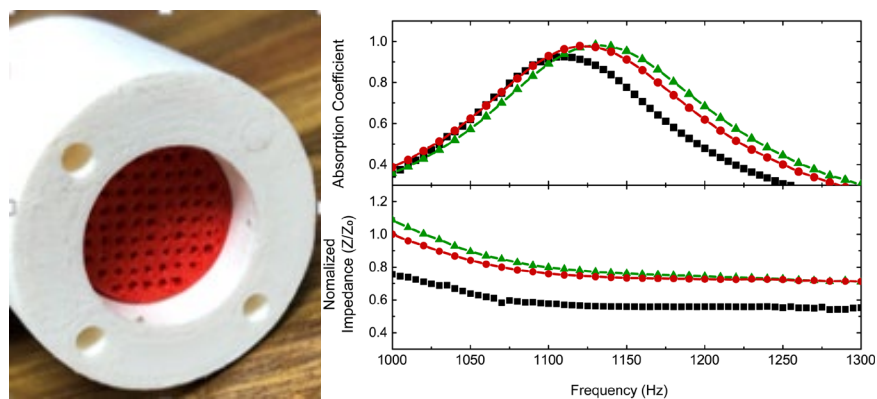


Figure 5.6: Experimental results for adding an MPP inside the cavity. (a) Photo of an MPP inside the cylindrical cavity; (b) absorption spectra for different diameters for the MPP hole (top); (bottom) three damping factors as a function of frequencies.

5.4.3 Tuning by Using Lighter Porous Materials (Silica Aerogel)

As discussed in Section 5.2, the absorption bandwidth increases as the equivalent mass decreases. Based on this prediction from the lumped model, a lighter material of silica aerogel, whose density is only 100 kg/m^2 , is used as the diaphragm material of AMM unit cells. As illustrated in Figure 5.7a, a cylindrical aerogel (purchased from

Buyaerogel.com) with 7-mm thickness and 13-mm radius is surrounded by a 3D-printed ring. Absorption spectra are measured for three cavity depths (10 mm, 20 mm, 30mm) and plot in Figure 5.7b. All three absorption bands have an incredibly broad band. Also, the bandwidth increases from 670 Hz, 690 Hz to 710 Hz as the air cavity lengths increases from 10 mm to 30 mm. It should be pointed out that the thickness of the silica aerogel disk is 7 mm, which is much larger than the polyimide diaphragm (50 μm). The mass per area of the aerogel film is five times larger (0.4 kg/m^2 vs 0.077 kg/m^2). In other words, the increase of absorption bandwidth should be attributed to the porous nature of the silica aerogel. Future experiments are planned to use thin film of silica aerogel that can potentially increase the bandwidth further.

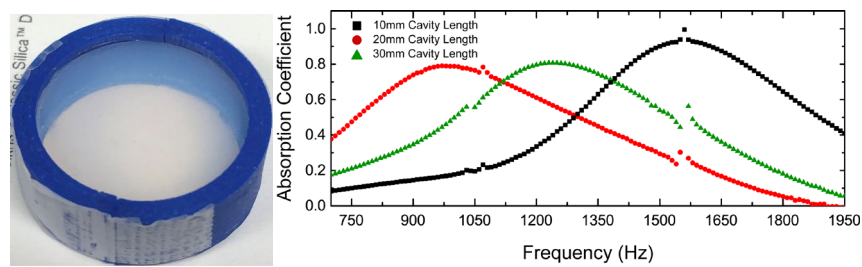


Figure 5.7: Preliminary experimental results for aerogel membrane.

5.5 Summary

Aiming to address the narrow bandwidth limitation in membrane-based AMM for acoustic absorption, in this paper, we first present a theoretical framework based on the impedance matching principle and describing the diaphragm-and-cavity combination

by an effective mass-spring-dashpot model. Through this model, we find that the key to realize large bandwidth is using a lighter diaphragm while maintaining the impedance matching condition. We then study three different approaches for tuning the effective damping of unit cells consisting of light and uniform diaphragm backed by an air cavity, including tuning the cavity length, static pressure, and an added thickness perforated plate. A preliminary experimental measurement is carried out based on the first approach and verifies that i) the effective damping coefficient of the diaphragm can indeed be tuned by changing the cavity length to ensure impedance matching, ii) using a lighter diaphragm can significantly increase the absorption bandwidth. Further efforts will be devoted to combine various unit cells to have even larger absorption bandwidth so that the developed AMM thin panel can be put into practical applications in noise control and mitigation.

CHAPTER 6: SUMMARY

Thrust 1: Understanding of acoustic-structural interaction

In this thrust, a large-scale pressure sensor, constructed by a thin diaphragm coupled with a tunable-backed cavity, has been used to study and verify how the acoustic-structural interaction changes the effective mass density of the diaphragm and as a result affects the sensitivity and bandwidth. Through the FEM simulation and experimental validation, it is found that as the length of the backing cavity decreases, the effective static sensitivity increases, but the fundamental natural frequency exhibits a unique three-stage trend: it increases in the extended cavity length range, saturates in the medium cavity length range, and decreases in the short cavity length range. This finding cannot be correctly modeled by the widely used lumped mechanical system. This thrust serves as starting theoretical guidance for Thrusts 2-4.

Thrust 2: Development of fiber optic sensor with air-backed graphene diaphragm

It is found through the study in Thrust 1 that the mechanical sensitivity of dynamic pressure sensors is limited by the air cavity when the cavity length is minimal. Aiming to improve the overall sensitivity of dynamic pressure sensors, two different methods have been adopted in the development of fiber optic sensors with air-backed graphene diaphragm. In the first approach, a graphene-silver composite diaphragm is used as a reflecting surface of the Fabry-Perot interferometer. Experiments show that it improves the optical sensitivity by a factor of three. In the second approach, the sensor is

redesigned with a large side gap, effectively increasing the volume of the backing air cavity. Experiments show that the mechanical sensitivity increases by an order of magnitude. These sensors serve as indispensable pressure probes with a small footprint but a high sensitivity.

Thrust 3: Development of acoustic sensors mimicking internally coupled ears

There is a fundamental challenge to develop miniature acoustic sensors for sound source localization due to the size constraint. To address this challenge, we seek to develop bio-inspired sensors mimicking the internally coupled ears found in many animals such as lizards. The developed sensor utilizes the acoustic-structural interaction to acoustically couple two eardrums via a U-shaped air cavity. A prototype has been developed, fabricated, and characterized, which shows that the internal coupling mechanism is able to amplify the small interaural phase difference by order of magnitude, which can only be obtained by a conventional microphone pair that is separated further by the same factor.

Thrust 4: Development of acoustic metamaterials with air-coupled diaphragms

Acoustic metamaterials have in recent years become an indispensable tool to develop materials with exotic acoustic properties. One challenge is to make a thin plate but with perfect absorption. Through analytical modeling and FEM simulation, it is found that ideal absorption can be achieved using an air-backed diaphragm by tuning i) the cavity length, ii) the pressure in the cavity, and iii) the damping through a perforated plate.

Preliminary experiments have demonstrated the feasibility of the first approach but for narrow bandwidth.

BIBLIOGRAPHY

Miles RN, Robert D, Hoy RR.1995. "Mechanically coupled ears for directional hearing in the parasitoid fly *Ormia ochracea*." *The Journal of the Acoustical Society of America*: 98(6):3059-3070. <https://doi.org/10.1121/1.413830>

Andrews, M., I. Harris, and G. Turner. 1993. "A Comparison of Squeeze-Film Theory with Measurements on a Microstructure." *Sensors and Actuators: A. Physical* 36 (1): 79–87. [https://doi.org/10.1016/0924-4247\(93\)80144-6](https://doi.org/10.1016/0924-4247(93)80144-6).

Antonsson, Erik K., and J. Cagan. "Microsystem design synthesis." Formal engineering design synthesis. Cambridge University Press, 2001. 126-169.

Bae, H, and M Yu. 2012. "Miniature Fabry-Perot Pressure Sensor Created by Using UV-Molding Process with an Optical Fiber Based Mold." *Optics Express* 20 (13): 14573–83. <https://doi.org/10.1364/OE.20.014573>.

Balandin, Alexander A, Suchismita Ghosh, Wenzhong Bao, Irene Calizo, Desalegne Teweldebrhan, Feng Miao, and Chun Ning Lau. 2008. "Superior Thermal Conductivity of Single-Layer Graphene." *Nano Letters* 8 (3): 902–7. <https://doi.org/10.1021/nl0731872>.

Bao, Minhang, and Heng Yang. 2007. "Squeeze Film Air Damping in MEMS." *Sensors and Actuators, A: Physical* 136 (1): 3–27. <https://doi.org/10.1016/j.sna.2007.01.008>.

Bao, Minhang, Heng Yang, Yuancheng Sun, and Paddy J. French. 2003. "Modified Reynolds' Equation and Analytical Analysis of Squeeze-Film Air Damping of

Perforated Structures.” *Journal of Micromechanics and Microengineering* 13 (6): 795–800. <https://doi.org/10.1088/0960-1317/13/6/301>.

Basu, S., and P. Bhattacharyya. 2012. “Recent Developments on Graphene and Graphene Oxide Based Solid State Gas Sensors.” *Sensors and Actuators, B: Chemical* 173: 1–21. <https://doi.org/10.1016/j.snb.2012.07.092>.

Bee, Mark A., and Jakob Christensen-Dalsgaard. 2016. “Sound Source Localization and Segregation with Internally Coupled Ears: The Treefrog Model.” *Biological Cybernetics* 110 (4–5): 271–90. <https://doi.org/10.1007/s00422-016-0695-5>.

Benesty, J., Chen, J. and Huang, Y., 2008. *Microphone array signal processing* (Vol. 1). Springer Science & Business Media.

Beranek, L L. 1954. “Sound Systems for Large Auditoriums.” *The Journal of the Acoustical Society of America* 26 (5): 661–75.

Bierman, Hilary S., Jennifer L. Thornton, Heath G. Jones, Kanthaiah Koka, Bruce A. Young, Christian Brandt, Jakob Christensen-Dalsgaard, Catherine E. Carr, and Daniel J. Tollin. 2014. “Biophysics of Directional Hearing in the American Alligator (*Alligator Mississippiensis*).” *Journal of Experimental Biology* 217 (7): 1094–1107. <https://doi.org/10.1242/jeb.092866>.

Blackstock, David T., and Anthony A. Atchley. 2001. “Fundamentals of Physical Acoustics.” *The Journal of the Acoustical Society of America* 109 (4): 1274–76. <https://doi.org/10.1121/1.1354982>.

Brandstein, Michael. 2001. *Microphone Arrays: Signal Processing Techniques and Applications*. Zhou, Xin, and Thomas Schoepf. 2012. "Detection and Formation Process of Overheated Electrical Joints Due to Faulty Connections." *IET Conference Publications 2012(605CP)*:288–95. <https://doi.org/10.1049/cp.2012.0663>. Zhang, Wenyi, and Bhaskar D. Rao. 20.

Carr, Catherine E., Jakob Christensen-Dalsgaard, and Hilary Bierman. 2016. "Coupled Ears in Lizards and Crocodylians." *Biological Cybernetics* 110 (4–5): 291–302. <https://doi.org/10.1007/s00422-016-0698-2>.

Castro Neto, A. H., F. Guinea, N. M.R. Peres, K. S. Novoselov, and A. K. Geim. 2009. "The Electronic Properties of Graphene." *Reviews of Modern Physics* 81 (1): 109–62. <https://doi.org/10.1103/RevModPhys.81.109>.

Chen, Xu-Dong, Zhi-Bo Liu, Chao-Yi Zheng, Fei Xing, Xiao-Qing Yan, Yongsheng Chen, and Jian-Guo Tian. 2013. "High-Quality and Efficient Transfer of Large-Area Graphene Films onto Different Substrates." *Carbon* 56 (May): 271–78. <https://doi.org/10.1016/j.carbon.2013.01.011>.

Cheng, C. I., and G. H. Wakefield. 2001. "Introduction to Head-Related Transfer Functions (HRTFs): Representations of HRTFs in Time, Frequency, and Space." *AES: Journal of the Audio Engineering Society* 49 (4): 231–49.

Christensen-Dalsgaard, Jakob, and Geoffrey A. Manley. 2005. "Directionality of the Lizard Ear." *Journal of Experimental Biology* 208 (6): 1209–17. <https://doi.org/10.1242/jeb.01511>.

Christensen-Dalsgaard, Jakob, and Geoffrey A. Manley. 2008. "Acoustical Coupling of Lizard Eardrums." *JARO - Journal of the Association for Research in Otolaryngology* 9 (4): 407–16. <https://doi.org/10.1007/s10162-008-0130-2>.

Christensen-Dalsgaard, Jakob, Yezhong Tang, and Catherine E. Carr. 2011. "Binaural Processing by the Gecko Auditory Periphery." *Journal of Neurophysiology* 105 (5): 1992–2004. <https://doi.org/10.1152/jn.00004.2011>.

Dahlin, Andreas B. 2012. "Size Matters: Problems and Advantages Associated with Highly Miniaturized Sensors." *Sensors* 12 (3): 3018–36. <https://doi.org/10.3390/s120303018>.

Silva, Clarence W. de. 2016. *Sensor Systems: Fundamentals and Applications*. 1st ed. Zhou, Xin, and Thomas Schoepf. 2012. "Detection and Formation Process of Overheated Electrical Joints Due to Faulty Connections." *IET Conference Publications* 2012 (605 CP): 288–95. <https://doi.org/10.1049/cp.2012.0663>. Zhang, Wenyi, and Bhaskar D. Rao. 20.

Diaphragm, Multilayer Graphene, Jun Ma, Haifeng Xuan, Hoi Lut Ho, Wei Jin, Yuanhong Yang, and Shangchun Fan. 2013. "Fiber-Optic Fabry – Pérot Acoustic Sensor With." *IEEE Photonics Technology Letters* 25 (10): 932–35.

Dong, Qian, Hyungdae Bae, Zhijian Zhang, Yongyao Chen, Zhongshan Wen, Douglas A. Olson, Miao Yu, and Haijun Liu. 2019. "Miniature Fiber Optic Acoustic Pressure Sensors with Air-Backed Graphene Diaphragms." *Journal of Vibration and Acoustics, Transactions of the ASME* 141 (4): 1–8. <https://doi.org/10.1115/1.4042929>.

Dooling, Robert J, Bernard Lohr, and Micheal L Dent. 2000. "Hearing in Birds and Reptiles." In *Comparative Hearing: Birds and Reptiles*, 308–59. Zhou, Xin, and Thomas Schoepf. 2012. "Detection and Formation Process of Overheated Electrical Joints Due to Faulty Connections." *IET Conference Publications 2012 (605 CP)*: 288–95. <https://doi.org/10.1049/cp.2012.0663>. Zhang, Wenyi, and Bhaskar D. Rao. 20.

Dowell, Earl H, G F Gorman Iii, and D A Smith. 1977. "Acoustoelasticity: General Theory, Acoustic Natural Modes and Forced Response to Sinusoidal Excitation, Including Comparisons with Experiment." *Journal of Sound and Vibration* 52 (4): 519–42.

Eaton, W. P., and J. H. Smith. 1997. "Micromachined Pressure Sensors: Review and Recent Developments." *Smart Materials and Structures* 6 (5): 530–39. <https://doi.org/10.1088/0964-1726/6/5/004>.

Fletcher, Neville H. 1992. *Acoustic Systems in Biology*. Zhou, Xin, and Thomas Schoepf. 2012. "Detection and Formation Process of Overheated Electrical Joints Due to Faulty Connections." *IET Conference Publications 2012 (605 CP)*: 288–95. <https://doi.org/10.1049/cp.2012.0663>. Zhang, Wenyi, and Bhaskar D. Rao. 20.

Fonseca, P. J., and R. M. Hennig. 2004. "Directional Characteristics of the Auditory System of Cicadas: Is the Sound Producing Tymbal an Integral Part of Directional Hearing?" *Physiological Entomology* 29 (4): 400–408. <https://doi.org/10.1111/j.0307-6962.2004.00408.x>.

Geim, A K. 2009. "Graphene: Status and Prospects." *Science (New York, N.Y.)* 324 (5934): 1530–34. <https://doi.org/10.1126/science.1158877>.

Geim, Andre K, and Konstantin S Novoselov. 2010. "The Rise of Graphene." In *Nanoscience and Technology: A Collection of Reviews from Nature Journals*, 11–19.

Zhou, Xin, and Thomas Schoepf. 2012. "Detection and Formation Process of Overheated Electrical Joints Due to Faulty Connections." *IET Conference Publications 2012 (605 CP)*: 288–95. <https://doi.org/10.1049/cp.2012.0663>. Zhang, Wenyi, and Bhaskar D. Rao. 20.

Gladwell, G M L, and G Zimmermann. 1966. "On Energy and Complementary Energy Formulations of Acoustic and Structural Vibration Problems." *Journal of Sound and Vibration* 3 (3): 233–41.

Gorman, D G, J M Reese, J Horáček, and K Dedouch. 2001. "Vibration Analysis of a Circular Disc Backed by a Cylindrical Cavity." *Proceedings of the Institution of Mechanical Engineers, Part C: Journal of Mechanical Engineering Science* 215 (11): 1303–11. <https://doi.org/10.1243/0954406011524685>.

Grattan, K T V, and T Sun. 2000. "Fiber Optic Sensor Technology: Introduction and Overview." In *Optical Fiber Sensor Technology*, 1–44.

Zhou, Xin, and Thomas Schoepf. 2012. "Detection and Formation Process of Overheated Electrical Joints Due to Faulty Connections." *IET Conference Publications 2012 (605 CP)*: 288–95. <https://doi.org/10.1049/cp.2012.0663>. Zhang, Wenyi, and Bhaskar D. Rao. 20.

Guy, R W. 1979. "The Response of a Cavity Backed Panel to External Airborne Excitation: A General Analysis." *The Journal of the Acoustical Society of America* 65 (3): 719–31.

Hall, Neal A, Murat Okandan, Robert Littrell, Baris Bicen, and F Levent Degertekin. 2007. "Micromachined Optical Microphone Structures with Low Thermal-

Mechanical Noise Levels.” *The Journal of the Acoustical Society of America* 122 (4): 2031–37.

Hernandez, Yenny, Valeria Nicolosi, Mustafa Lotya, Fiona M Blighe, Zhenyu Sun, Sukanta De, I T McGovern, et al. 2008. “High-Yield Production of Graphene by Liquid-Phase Exfoliation of Graphite.” *Nature Nanotechnology* 3 (9): 563–68.
<https://doi.org/10.1038/nnano.2008.215>.

Hierold, Christofer. 2004. “From Micro- to Nanosystems: Mechanical Sensors Go Nano.” *Journal of Micromechanics and Microengineering* 14 (9).
<https://doi.org/10.1088/0960-1317/14/9/001>.

Hill, Ernie W., Aravind Vijayaraghavan, and Kostya Novoselov. 2011. “Graphene Sensors.” *IEEE Sensors Journal* 11 (12): 3161–70
<https://doi.org/10.1109/JSEN.2011.2167608>.

Homentcovschi, Dorel, and R. N. Miles. 2005. “Viscous Damping of Perforated Planar Micromechanical Structures.” *Sensors and Actuators, A: Physical* 119 (2): 544–52. <https://doi.org/10.1016/j.sna.2004.10.032>.

Hou, Max Ti Kuang, and Rongshun Chen. 2004. “A New Residual Stress Measurement Method Using Ultra-Wide Micromachined Bilayer Cantilevers.” *Journal of Micromechanics and Microengineering* 14 (4): 490–96.
<https://doi.org/10.1088/0960-1317/14/4/008>.

K. S. Novoselov, A. K. Geim, S. V. Morozov, D. Jiang, Y. Zhang, S. V. Dubonos, I. V. Grigorieva and A. A. Firsov. 2016. “Electric Field Effect in Atomically Thin Carbon Films” *306 (5696): 666–69*.

Kahng, Yung Ho, Sangchul Lee, Woojin Park, Gunho Jo, Minhyeok Choe, Jong-Hoon Lee, Hyunung Yu, Takhee Lee, and Kwanghee Lee. 2012. "Thermal Stability of Multilayer Graphene Films Synthesized by Chemical Vapor Deposition and Stained by Metallic Impurities." *Nanotechnology* 23 (7): 075702. <https://doi.org/10.1088/0957-4484/23/7/075702>.

Kaina, Nadège, Fabrice Lemoult, Mathias Fink, and Geoffroy Lerosey. 2015. "Negative Refractive Index and Acoustic Superlens from Multiple Scattering in Single Negative Metamaterials." *Nature* 525 (7567): 77–81. <https://doi.org/10.1038/nature14678>.

Kettler, Lutz, Jakob Christensen-Dalsgaard, Ole Næsbye Larsen, and Hermann Wagner. 2016. "Low Frequency Eardrum Directionality in the Barn Owl Induced by Sound Transmission through the Interaural Canal." *Biological Cybernetics* 110 (4–5): 333–43. <https://doi.org/10.1007/s00422-016-0689-3>.

Kim, Kwanpyo, William Regan, Baisong Geng, Benjamín Alemán, B. M. Kessler, Feng Wang, M. F. Crommie, and A. Zettl. 2010. "High-Temperature Stability of Suspended Single-Layer Graphene." *Physica Status Solidi (RRL) - Rapid Research Letters* 4 (11): 302–4. <https://doi.org/10.1002/pssr.201000244>.

Ko, Sang Choon, Yong Chul Kim, Seung Seob Lee, Seung Ho Choi, and Sang Ryong Kim. 2003. "Micromachined Piezoelectric Membrane Acoustic Device." *Sensors and Actuators, A: Physical* 103 (1–2): 130–34. [https://doi.org/10.1016/S0924-4247\(02\)00310-2](https://doi.org/10.1016/S0924-4247(02)00310-2).

Koenig, Steven P, Narasimha G Boddeti, Martin L Dunn, and J Scott Bunch. 2011. "Ultrastrong Adhesion of Graphene Membranes." *Nature Nanotechnology* 6 (9): 543–46. <https://doi.org/10.1038/nnano.2011.123>.

Kshetrimayum, Rakesh S. 2004. "A Brief Intro to Metamaterials." *IEEE Potentials* 23 (5): 44–46. <https://doi.org/10.1109/MP.2005.1368916>.

Kuila, Tapas, Saswata Bose, Partha Khanra, Ananta Kumar Mishra, Nam Hoon Kim, and Joong Hee Lee. 2011. "Recent Advances in Graphene-Based Biosensors." *Biosensors and Bioelectronics* 26 (12): 4637–48. <https://doi.org/10.1016/j.bios.2011.05.039>.

Larsen, Ole Næsbye, Jakob Christensen-Dalsgaard, and Kenneth Kragh Jensen. 2016. "Role of Intracranial Cavities in Avian Directional Hearing." *Biological Cybernetics* 110 (4–5): 319–31. <https://doi.org/10.1007/s00422-016-0688-4>.

Van Suu, Thierry Le, Stéphane Durand, and Michel Bruneau. 2010. "On the Modelling of Clamped Plates Loaded by a Squeeze Fluid Film: Application to Miniaturised Sensors." *Acta Acustica United with Acustica* 96 (5): 923–35. <https://doi.org/10.3813/AAA.918351>.

Lee, Changgu, Xiaoding Wei, Jeffrey W Kysar, and James Hone. 2008. "Of Monolayer Graphene" 321 (July): 385–88.

Lee, Seung Mok, Bu Sang Cha, and Masanori Okuyama. 2010. "The Influence of Acoustic Damping on the Transformation Efficiency of Capacitive Micromachined Ultrasonic Transducer in Air." *Journal of Applied Physics* 108 (7). <https://doi.org/10.1063/1.3481418>.

Li, Cheng, Jun Xiao, Tingting Guo, Shangchun Fan, and Wei Jin. 2015. "Interference Characteristics in a Fabry–Perot Cavity with Graphene Membrane for Optical Fiber Pressure Sensors." *Microsystem Technologies* 21 (11): 2297–2306. <https://doi.org/10.1007/s00542-014-2333-2>.

Li, Jensen, and C. T. Chan. 2004. "Double-Negative Acoustic Metamaterial." *Physical Review E - Statistical Physics, Plasmas, Fluids, and Related Interdisciplinary Topics* 70 (5): 4. <https://doi.org/10.1103/PhysRevE.70.055602>.

Li, Xuesong, Weiwei Cai, Jinho An, Seyoung Kim, Junghyo Nah, Dongxing Yang, Richard Piner, et al. 2009. "Large-Area Synthesis of High-Quality and Uniform Graphene Films on Copper Foils." *Science* 324 (5932): 1312–14. <https://doi.org/10.1126/science.1171245>.

Li, Xuesong, Yanwu Zhu, Weiwei Cai, Mark Borysiak, Boyang Han, David Chen, Richard D Piner, Luigi Colombo, and Rodney S Ruoff. 2009. "Transfer of Large-Area Graphene Films for High-Performance Transparent Conductive Electrodes." *Nano Letters* 9 (12): 4359–63. <https://doi.org/10.1021/nl902623y>.

Li, Yong, Bin Liang, Zhong Ming Gu, Xin Ye Zou, and Jian Chun Cheng. 2013. "Reflected Wavefront Manipulation Based on Ultrathin Planar Acoustic Metasurfaces." *Scientific Reports* 3. <https://doi.org/10.1038/srep02546>.

Liao, Yunhong, Xiaoming Zhou, Yangyang Chen, and Guoliang Huang. 2019. "Adaptive Metamaterials for Broadband Sound Absorption at Low Frequencies." *Smart Materials and Structures* 28 (2). <https://doi.org/10.1088/1361-665X/aaeceb>.

Lin, Y. M., C. Dimitrakopoulos, K. A. Jenkins, D. B. Farmer, H. Y. Chiu, A. Grill, and Ph Avouris. 2010. "100-GHz Transistors from Wafer-Scale Epitaxial Graphene." *Science* 327 (5966): 662. <https://doi.org/10.1126/science.1184289>.

Lin, Yu Ming, Alberto Valdes-Garcia, Shu Jen Han, Damon B. Farmer, Inanc Meric, Yanning Sun, Yanqing Wu, et al. 2011. "Wafer-Scale Graphene Integrated Circuit." *Science* 332 (6035): 1294–97. <https://doi.org/10.1126/science.1204428>.

- Liu, Haijun, Luke Currano, Danny Gee, Tristan Helms, and Miao Yu. 2013. "Understanding and Mimicking the Dual Optimality of the Fly Ear." *Scientific Reports* 3. <https://doi.org/10.1038/srep02489>.
- Liu, Haijun, Douglas A. Olson, and Miao Yu. 2014. "Modeling of an Air-Backed Diaphragm in Dynamic Pressure Sensors: Effects of the Air Cavity." *Journal of Sound and Vibration* 333 (25): 7051–75. <https://doi.org/10.1016/j.jsv.2014.07.004>.
- Lock, Evgeniya H, Mira Baraket, Matthew Laskoski, Shawn P Mulvaney, Woo K Lee, Paul E Sheehan, Daniel R Hines, et al. 2012. "High-Quality Uniform Dry Transfer of Graphene to Polymers." *Nano Letters* 12 (1): 102–7. <https://doi.org/10.1021/nl203058s>.
- Loh, Kian Ping, Qiaoliang Bao, Priscilla Kailian Ang, and Jiaxiang Yang. 2010. "The Chemistry of Graphene." *Journal of Materials Chemistry* 20 (12): 2277. <https://doi.org/10.1039/b920539j>.
- Lomax, H, TH Pulliam, DW Zingg, and TA Kowalewski. 2002. "Fundamentals of Computational Fluid Dynamics." *Applied Mechanics Reviews* 55 (4): B61. <https://doi.org/10.1115/1.1483340>.
- M. Christopher, A. Melnick L. Sheng. 2016. "乳鼠心肌提取 HHS Public Access." *Physiology & Behavior* 176 (1): 100–106. <https://doi.org/10.1016/j.heares.2015.05.009.Sound>.
- Ma, Fuyin, Jiu Hui Wu, Meng Huang, Weiquan Zhang, and Siwen Zhang. 2015. "A Purely Flexible Lightweight Membrane-Type Acoustic Metamaterial." *Journal of*

Physics D: Applied Physics 48 (17). <https://doi.org/10.1088/0022-3727/48/17/175105>.

Ma, Guancong, and Ping Sheng. 2016. “Acoustic Metamaterials: From Local Resonances to Broad Horizons.” *Science Advances* 2 (2). <https://doi.org/10.1126/sciadv.1501595>.

Ma, Guancong, Min Yang, Songwen Xiao, Zhiyu Yang, and Ping Sheng. 2014. “Acoustic Metasurface with Hybrid Resonances.” *Nature Materials* 13 (9): 873–78. <https://doi.org/10.1038/nmat3994>.

Ma, Jun, Wei Jin, Hoi Lut Ho, and Ji Yan Dai. 2012. “High-Sensitivity Fiber-Tip Pressure Sensor with Graphene Diaphragm.” *Optics Letters* 37 (13): 2493–95.

Marti, Amparo, Maximo Cobos, and Jose J. Lopez. 2011. “Real Time Speaker Localization and Detection System for Camera Steering in Multiparticipant Videoconferencing Environments.” *ICASSP, IEEE International Conference on Acoustics, Speech and Signal Processing - Proceedings*, 2592–95. <https://doi.org/10.1109/ICASSP.2011.5947015>.

Mason, Andrew C., Michael L. Oshinsky, and Ron R. Hoy. 2001. “Hyperacute Directional Hearing in a Microscale Auditory System.” *Nature* 410 (6829): 686–90. <https://doi.org/10.1038/35070564>.

Michelsen, A., and K. Rohrseitz. 1995. “Directional Sound Processing and Interaural Sound Transmission in a Small and a Large Grasshopper.” *Journal of Experimental Biology* 198 (9): 1817–27.

Michelsen, A., K. Rohrseitz, K. G. Heller, and A. Stumpner. 1994. "A New Biophysical Method to Determine the Gain of the Acoustic Trachea in Bushcrickets." *Journal of Comparative Physiology A* 175 (2): 145–51.
<https://doi.org/10.1007/BF00215110>.

Miles, R. N., Q. Su, W. Cui, M. Shetye, F. L. Degertekin, B. Bicen, C. Garcia, S. Jones, and N. Hall. 2009. "A Low-Noise Differential Microphone Inspired by the Ears of the Parasitoid Fly *Ormia ochracea*." *The Journal of the Acoustical Society of America* 125 (4): 2013–26. <https://doi.org/10.1121/1.3082118>.

Milton, Graeme W., and John R. Willis. 2007. "On Modifications of Newton's Second Law and Linear Continuum Elastodynamics." *Proceedings of the Royal Society A: Mathematical, Physical and Engineering Sciences* 463 (2079): 855–80.
<https://doi.org/10.1098/rspa.2006.1795>.

Narins, Peter M. 2016. "ICE on the Road to Auditory Sensitivity Reduction and Sound Localization in the Frog." *Biological Cybernetics* 110 (4–5): 263–70.
<https://doi.org/10.1007/s00422-016-0700-z>.

Novoselov, K S, A K Geim, S V Morozov, D Jiang, M I Katsnelson, I V Grigorieva, S V Dubonos, and A A Firsov. 2005. "Two-Dimensional Gas of Massless Dirac Fermions in Graphene." *Nature* 438 (7065): 197–200.
<https://doi.org/10.1038/nature04233>.

Novoselov, K S, D Jiang, F Schedin, T J Booth, V V Khotkevich, S V Morozov, and A K Geim. 2005. "Two-Dimensional Atomic Crystals." *Proceedings of the National Academy of Sciences of the United States of America* 102 (30): 10451–53.
<https://doi.org/10.1073/pnas.0502848102>.

Pan, Jie. 1992. "The Forced Response of an Acoustic-structural Coupled System." *The Journal of the Acoustical Society of America* 91 (2): 949–56.

Pedersen, Michael, Wouter Olthuis, and Piet Bergveld. 1997. "A Silicon Condenser Microphone with Polyimide Diaphragm and Backplate." *Sensors and Actuators, A: Physical* 63 (2): 97–104. [https://doi.org/10.1016/S0924-4247\(97\)01532-X](https://doi.org/10.1016/S0924-4247(97)01532-X).

Poot, M., and H. S.J. Van Der Zant. 2008. "Nanomechanical Properties of Few-Layer Graphene Membranes." *Applied Physics Letters* 92 (6). <https://doi.org/10.1063/1.2857472>.

Pourmohammad, Ali, and Seyed Mohammad Ahadi. 2013. "N -Dimensional N - Microphone Sound Source Localization," 1–19.

Pretlove, A J. 1965. "Free Vibrations of a Rectangular Panel Backed by a Closed Rectangular Cavity by a Closed Rectangular Cavity." *Journal of Sound and Vibration* 2 (3): 197–209.

Pretlove, A J, and A Craggs. 1970. "A Simple Approach to Coupled Panel-Cavity Vibrations." *Journal of Sound and Vibration* 11 (2): 207-IN1.

Qaisi, Mazen I. 1988. "Free Vibrations of a Rectangular Plate-Cavity System." *Applied Acoustics* 24 (1): 49–61.

Rajalingham, C, R B Bhat, and G D Xistris. 1995. "Natural Vibration of a Cavity Backed Rectangular Plate Using a Receptor-Rejector System Model."

Rajalingham, C, R B Bhat, and G D Xistris. 1998. "Vibration of Circular Membrane Backed by Cylindrical Cavity." *International Journal of Mechanical Sciences* 40 (8): 723–34.

Reina, Alfonso, Xiaoting Jia, John Ho, Daniel Nezich, Hyungbin Son, Vladimir Bulovic, Mildred S Dresselhaus, and Jing Kong. 2009. "Large Area, Few-Layer Graphene Films on Arbitrary Substrates by Chemical Vapor Deposition." *Nano Letters* 9 (1): 30–35. <https://doi.org/10.1021/nl801827v>.

Ried, Robert Paul. 1994. "Micromachined piezoelectric microphones." PhD diss., University of California, Berkeley.

Römer, Heiner, and Arne K.D. Schmidt. 2016. "Directional Hearing in Insects with Internally Coupled Ears." *Biological Cybernetics* 110 (4–5): 247–54. <https://doi.org/10.1007/s00422-015-0672-4>.

Schedin, F., A. K. Geim, S. V. Morozov, E. W. Hill, P. Blake, M. I. Katsnelson, and K. S. Novoselov. 2007. "Detection of Individual Gas Molecules Adsorbed on Graphene." *Nature Materials* 6 (9): 652–55. <https://doi.org/10.1038/nmat1967>.

Scheeper, P. R., W. Olthuis, and P. Bergveld. 1992. "A Silicon Condenser Microphone with a Silicon Nitride Diaphragm and Backplate." *Journal of Micromechanics and Microengineering* 2 (3): 187–89. <https://doi.org/10.1088/0960-1317/2/3/016>.

Scheeper, Patrick Richard, Børge Nordstrand, Jens Ole Gulløy, Bin Liu, Thomas Clausen, Lise Midjord, and Torben Storgaard-Larsen. 2003. "A New Measurement Microphone Based on MEMS Technology." *Journal of Microelectromechanical Systems* 12 (6): 880–91. <https://doi.org/10.1109/JMEMS.2003.820260>.

Schellin, R., and G. Hess. 1992. "A Silicon Subminiature Microphone Based on Piezoresistive Polysilicon Strain Gauges." *Sensors and Actuators: A. Physical* 32 (1–3): 555–59. [https://doi.org/10.1016/0924-4247\(92\)80043-3](https://doi.org/10.1016/0924-4247(92)80043-3).

Schmidt, Arne K.D., and Heiner Römer. 2013. "Diversity of Acoustic Tracheal System and Its Role for Directional Hearing in Crickets." *Frontiers in Zoology* 10 (1): 1–9. <https://doi.org/10.1186/1742-9994-10-61>.

Shelby, R. A., D. R. Smith, and S. Schultz. 2001. "Experimental Verification of a Negative Index of Refraction." *Science* 292 (5514): 77–79. <https://doi.org/10.1126/science.1058847>.

Sheng, Ping, X. X. Zhang, Z. Liu, and C. T. Chan. 2003. "Locally Resonant Sonic Materials." *Physica B: Condensed Matter* 338 (1–4): 201–5. [https://doi.org/10.1016/S0921-4526\(03\)00487-3](https://doi.org/10.1016/S0921-4526(03)00487-3).

Škvor, Z. 1969. "On the Acoustical Resistance Due to Viscous Losses in the Air Gap of Electrotastic Transducers." *Ultrasonics* 7: 83.

Škvor, Z. 1967. "On the Acoustical Resistance Due to Viscous Losses in the Air Gap of Electrostatic Transducers." *Acta Acustica United with Acustica* 19 (5): 295–99.

Smith, Anderson.D., Sam Vaziri, Frank Niklaus, Andreas.C. Fischer, Mikael Sterner, Anna Delin, Mikael Östling, and Max.C. Lemme. 2013. "Pressure Sensors Based on Suspended Graphene Membranes." *Solid-State Electronics* 88 (October): 89–94. <https://doi.org/10.1016/j.sse.2013.04.019>.

Smith, David R., and Norman Kroll. 2000. "Negative Refractive Index in Left-Handed Materials." *Physical Review Letters* 85 (14): 2933–36.

<https://doi.org/10.1103/PhysRevLett.85.2933>.

Suk, Ji Won, Alexander Kitt, Carl W Magnuson, Yufeng Hao, Samir Ahmed, Junho An, Anna K Swan, Bennett B Goldberg, and Rodney S Ruoff. 2011. "Transfer of CVD-Grown Monolayer Graphene onto Arbitrary Substrates." *ACS Nano* 5 (9): 6916–24. <https://doi.org/10.1021/nn201207c>.

Weinstein, Ehud. 1982. "Optimal Source Localization and Tracking from Passive Array Measurements." *IEEE Transactions on Acoustics, Speech, and Signal Processing* 30 (1): 69–76. <https://doi.org/10.1109/TASSP.1982.1163855>.

Wever, Ernest Glen. 2019. *The Reptile Ear*. Vol. 5346. Zhou, Xin, and Thomas Schoepf. 2012. "Detection and Formation Process of Overheated Electrical Joints Due to Faulty Connections." *IET Conference Publications 2012 (605 CP)*: 288–95. <https://doi.org/10.1049/cp.2012.0663>. Zhang, Wenyi, and Bhaskar D. Rao. 20.

Wu, Kai, and Andy W H Khong. 2016. "Sound Source Localization and Tracking." In *Context Aware Human-Robot and Human-Agent Interaction*, 55–78. Zhou, Xin, and Thomas Schoepf. 2012. "Detection and Formation Process of Overheated Electrical Joints Due to Faulty Connections." *IET Conference Publications 2012 (605 CP)*: 288–95. <https://doi.org/10.1049/cp.2012.0663>. Zhang, Wenyi, and Bhaskar D. Rao. 20.

Wu, Ying, Yun Lai, and Zhao Qing Zhang. 2011. "Elastic Metamaterials with Simultaneously Negative Effective Shear Modulus and Mass Density." *Physical Review Letters* 107 (10): 1–5. <https://doi.org/10.1103/PhysRevLett.107.105506>.

Xu, Zhengyuan, Ning Liu, and Brian M. Sadler. 2007. "A Simple Closed-Form Linear Source Localization Algorithm." Proceedings - IEEE Military Communications Conference MILCOM. <https://doi.org/10.1109/MILCOM.2007.4454975>.

Yablonovitch, E., and T. J. Gmitter. 1989. "Photonic Band Structure: The Face-Centered-Cubic Case." *Physical Review Letters* 63 (18): 1950–53. <https://doi.org/10.1103/PhysRevLett.63.1950>.

Yang, Z., Jun Mei, Min Yang, N. H. Chan, and Ping Sheng. 2008. "Membrane-Type Acoustic Metamaterial with Negative Dynamic Mass." *Physical Review Letters* 101 (20): 1–4. <https://doi.org/10.1103/PhysRevLett.101.204301>.

Yao, Shanshan, Xiaoming Zhou, and Gengkai Hu. 2010. "Investigation of the Negative-Mass Behaviors Occurring below a Cut-off Frequency." *New Journal of Physics* 12. <https://doi.org/10.1088/1367-2630/12/10/103025>.

Yu, M., and B. Balachandran. 2005. "Sensor Diaphragm under Initial Tension: Linear Analysis." *Experimental Mechanics* 45 (2): 123–29. <https://doi.org/10.1177/0014485105052319>.

Yu, Miao, B Balachandran, and X.-H. Long. 2005. "Nonlinear Analysis of Sensor Diaphragm under Initial Tension." In *Proc.SPIE*. Vol. 5757. Zhou, Xin, and Thomas Schoepf. 2012. "Detection and Formation Process of Overheated Electrical Joints Due to Faulty Connections." *IET Conference Publications* 2012 (605 CP): 288–95. <https://doi.org/10.1049/cp.2012.0663>. Zhang, Wenyi, and Bhaskar D. Rao. 20. <https://doi.org/10.1117/12.599945>.

Yu, Miao, and Balakumar Balachandran. 2003. "Acoustic Measurements Using a Fiber Optic Sensor System." *Journal of Intelligent Materials Systems and Structures* 14 (7): 409–14. <https://doi.org/10.1177/1045389X03034058>.

Zhang, Shu, Chunguang Xia, and Nicholas Fang. 2011. "Broadband Acoustic Cloak for Ultrasound Waves." *Physical Review Letters* 106 (2): 1–4. <https://doi.org/10.1103/PhysRevLett.106.024301>.

Zhang, Wenyi, and Bhaskar D. Rao. 2010. "A Two Microphone-Based Approach for Source Localization of Multiple Speech Sources." *IEEE Transactions on Audio, Speech and Language Processing* 18 (8): 1913–28. <https://doi.org/10.1109/TASL.2010.2040525>.

Zhou, Xin, and Thomas Schoepf. 2012. "Detection and Formation Process of Overheated Electrical Joints Due to Faulty Connections." *IET Conference Publications* 2012 (605 CP): 288–95. <https://doi.org/10.1049/cp.2012.0663>.